THE ASTROPHYSICAL JOURNAL, 470:444–459, 1996 October 10

EVIDENCE FOR A MASSIVE BLACK HOLE IN THE ACTIVE GALAXY NGC 4261 FROM *HUBBLE SPACE TELESCOPE* IMAGES AND SPECTRA[1,2]

LAURA FERRARESE
Johns Hopkins University and Space Telescope Science Institute, Baltimore, MD 21218
HOLLAND C. FORD
Johns Hopkins University and Space Telescope Science Institute, Baltimore, MD 21218
AND
WALTER JAFFE
Leiden Observatory, PB 9513, Leiden, 2300 RA, Netherlands
Received 1995 October 30; accepted 1996 April 22

ABSTRACT

We present *HST*/WFPC2 *V*, *R*, and *I* images and *Hubble Space Telescope*/FOS spectra of the active galaxy NGC 4261. The galaxy hosts a nuclear disk of dust (see papers by Jaffe et al.), roughly perpendicular to the radio jet. The images presented here show evidence of a spiral-like structure in the disk that likely provides the means by which angular momentum is carried from the center outward, allowing the inner material to sink in. The disk is not in an equilibrium configuration: it is not coaxial with the major axis of the galaxy, and it is not centered on either the nucleus or on the isophotal center of the galaxy. This prompted us to conclude that the dust has probably an external origin. With respect to the isophotal center of the galaxy, the nucleus is displaced by about 3 pc (assuming a distance to NGC 4261 of 30 Mpc) in the direction of the radio lobes: such a displacement can be due to recoil from the radio jet. An Hα map of the nuclear region is obtained from the *R*-band image by using the *V* and *I* images for the continuum determination. The ionized gas is concentrated in a resolved region with a FWHM of 0″.12, or 17 pc. FOS spectra were taken with the 0″.1 aperture in the wavelength region between 4570 and 6870 Å, in a grid of 13 aperture positions around and at the nuclear location. The [N II] λλ6548, 6584 + Hα emission complex is detected at all but three of the aperture positions. Fainter emission in Hβ, [O III] λλ4459, 5007, [O I] λλ6300, 6364, [S II] λλ6717, 6731, [N I] λλ5200, 5202 and [N II] λ5756 is also detected. The central velocities of the [N II] lines as a function of distance from the center can be accounted for by assuming that the ionized gas is confined in a disk in Keplerian motion around a central mass $(4.9 \pm 1.0) \times 10^8\ M_\odot$. By integrating the unreddened *V* luminosity density we find a mass to light ratio $(M/L)_V \sim 2100\ M_\odot/L_\odot$ within the inner 14.5 pc. The large mass-to-light ratio, and the fact that NGC 4261 *is* a relatively strong radio galaxy, lead us to conclude that the majority of the central mass is concentrated in a $(4.9 \pm 1.0) \times 10^8\ M_\odot$ black hole.

Subject headings: black hole physics — galaxies: individual (NGC 4261) — galaxies: kinematics and dynamics — galaxies: nuclei

1. INTRODUCTION

The most widely accepted model for the energy production in active galactic nuclei (AGNs) is that of a massive black hole feeding from an accretion disk and converting a fraction of the mass of the accreted material into jets, radio, and X-ray emission. This model is supported by theoretical arguments (e.g., Blandford & Rees 1992 for a review), but until recently had only controversial and circumstantial observational support. However, recent *Hubble Space Telescope* (*HST*) and VLBA observations have shown that accretion disks do exist and that massive black holes are active in galactic nuclei (Jaffe et al. 1993; Ford et al. 1994; Harms et al. 1994; Miyoshi et al. 1995). As Kormendy & Richstone (1995) have stressed in their excellent review, with kinematic observations pointing to the presence of central dark objects with masses $M \sim 10^6$–$10^{9.5}\ M_\odot$ in eight E–Sbc galaxies, the search for massive black holes is moving from confirmation of their existence to demographics: what percentage of galaxies harbors massive black holes, how do the black hole masses correlate with nuclear activity and with galaxy morphology (brightness profile, total luminosity, etc.), how are the central engines fed, and, finally, how do the engines work in detail.

Since the seminal papers by Sargent et al. (1978) and Young et al. (1979), astronomers have tried to establish the existence and masses of central black holes by measuring the rotation and velocity dispersion of stars near the nucleus. Although the method yields highly suggestive mass-to-light ratios in rotationally supported, flattened galaxies such as NGC 3115 ($M/L > 50$ for $r < 0''.3$) and M104 ($M/L \sim 100$ for $r < 0''.3$), which have bright, rotating central stellar disks (Kormendy & Richstone 1992; Kormendy 1988; Kormendy et al. 1996), the method suffers from the limits imposed by the low stellar surface brightness in pressure-supported giant ellipticals, and from the ambiguities in interpreting stellar dispersion measurements (e.g., Richstone & Tremaine 1985).

An alternative to stellar dynamical studies is provided by the exploration of gas dynamics. Recent *HST* Wide Field and Planetary Camera 2 (WFPC2) Hα images of 3C 274 = M87, the brightest radio galaxy in the Virgo cluster,

---

[1] Paper submitted by L. F. to the Johns Hopkins University in partial fulfillment of the requirements for the degree of Doctor of Philosophy.

[2] Based on observations with the NASA/ESA *Hubble Space Telescope* obtained at the Space Telescope Science Institute, which is operated by AURA, Inc. under NASA contract No. NAS 5-26555.

have unveiled the presence of a 100 pc (assuming a distance to Virgo of 15 Mpc; Jacoby et al. 1989; Ferrarese et al. 1996a) nuclear disk of ionized gas and dust aligned with the large-scale radio jet (Ford et al. 1994). In contrast to stellar absorption lines, the bright emission lines of the disk can be easily and accurately measured. *HST* Faint Object Spectrograph (FOS) spectra have shown that the nuclear disk is in circular motion. This led to a successful determination of a central mass of $\sim(2.4 \pm 0.7) \times 10^9\ M_\odot$ interior to 0."25 (18 pc) and a mass-to-light ratio $(M/L)_I = 170$ (Harms et al. 1994).

M87 is not an isolated case. The high resolution of *HST*/WFPC allowed the study and, in many cases, the discovery of gas and dust in the nuclei of many elliptical galaxies (Jaffe et al. 1994; Lauer et al. 1995; O'Neil et al. 1994). NGC 4374, the second brightest radio galaxy in Virgo, harbors two dust lanes about 14 pc wide and 20 pc long; one of the two lanes crosses the bright unresolved stellar nucleus, the other runs parellel to the first ~60 pc to the north, and both are perpendicular to the kiloparsec-scale radio jets (Jaffe et al. 1994). Ground-based spectra (Ferrarese et al. 1996b) along the major, minor, and an intermediate axis, show the clear signature of rotation, even if lacking the necessary spatial resolution to allow an unambiguous detection of a central black hole. Another case, the elliptical galaxy NGC 6251, host of the spectacular radio source 1936+8240 (Waggett, Warner, & Baldwin 1977), harbors a small dust disk (O'Neil et al. 1994) surrounding a bright unresolved nucleus. As is the case for M87 and NGC 4374, the minor axis of the disk is aligned with the impressive 100 kpc radio jet and the axis of the megaparsec scale radio lobes. No *HST* spectroscopic observations of the nuclear region of this galaxy have yet been attempted.

It is interesting to note that, in all the cases detected so far, the minor axes of the disks are aligned with the radio jets, even when the direction of the jet is perpendicular to the galaxy spin axis (as in NGC 4261; Davis & Birkinshaw 1986). This fact, and the continuity of the ionized gas and/or dust into the active nucleus, suggest that the disks are intimately connected with the mechanism aligning the jets. The disks are obvious reservoirs of fuel for the central engines and may determine the direction of the jets by defining the angular momentum in the accretion disk.

This paper deals with another such interesting galaxy: the giant elliptical NGC 4261. The galaxy is the optical counterpart of the radio source 3C 270 (Birkinshaw & Davies 1985). The radio structure consists of an unresolved component at the location of the galaxy nucleus, and two radio lobes extending out to 4′ from the nucleus in a direction roughly perpendicular to the major axis of the galaxy. NGC 4261 projects onto the Virgo W cloud. Nolthenius (1993) studied the optical and velocity structure in the Virgo cluster region using the CfA1 sample of galaxies (Huchra et al. 1983) and concluded that NGC 4261 is the dominant member of a group of 33 galaxies located at twice the distance of Virgo. We therefore adopt 30 Mpc as the distance to NGC 4261. Prerefurbishment *HST*/WFPC images of NGC 4261 revealed a sharply defined disk of dust, 240 pc in diameter, whose minor axis is roughly aligned with the radio axis of the galaxy (Jaffe et al. 1993). Hα, [N II], and [S II] emission lines have been detected in the nuclear region (Kim 1989), and the gas dynamics have been studied in detail by Jaffe et al. (1996) using high-resolution ground-based spectra obtained at the William Herschel Telescope. The spectra show strong Hα, [S II], and [N II] emission lines with narrow cores and unusually broad bases. From the analysis of both the rotation curve along the major axis, and the broad wings of the forbidden lines, Jaffe et al. (1996) conclude that their observations are consistent with the presence of a nuclear black hole with a mass approximately $8 \times 10^7\ M_\odot$ (correcting Jaffe's et al. distance to 30 Mpc), even though the detection is far from being unambiguous because of the insufficient spatial resolution of the spectroscopic data and because of seeing effects.

In this paper, we present new *HST*/WFPC2 *V*, *R*, and *I* images and *HST*/FOS spectra of NGC 4261. Since the *R* filter transmits the Hα + [N II] emission lines, we derived a pure emission Hα image by using the *V* and *I* exposures as continuum images. The Hα image is used to study the morphology and luminosity of the ionized gas in the nuclear region. The postrefurbishment *HST V* and *I* images allow a more detailed study of the structure in the dust disk than could be done by Jaffe et al. (1996) and provide important information on the properties of the stellar population in the core of the galaxy. The *HST*/FOS spectra reveal that the ionized gas in the nuclear region is in circular motion, and point to the presence of a central mass $\sim(4.9 \pm 1.0) \times 10^8\ M_\odot$ inside 0."1 (15 pc). The corresponding mass-to-light ratio is $(M/L)_V \sim 2 \times 10^3\ M_\odot/L_\odot$, leading us to conclude that we have another—but no less exciting—nuclear massive black hole.

The plan of this paper is as follows: § 2 describes the observations and data reduction. Section 3 discusses the *V*, *R*, and *I* morphology, the $V-R$ and $V-I$ colors, and the properties of the Hα emission. The reader interested mainly in the calculation of the central mass can skim § 3 and read about the FOS observations and the kinematic models in § 4. Conclusions can be found in § 5.

2. OBSERVATIONS AND DATA REDUCTION

2.1. *WFPC2 Observations*

NGC 4261 was imaged on 1994 December 12 and 13, using the Wide Field and Planetary Camera 2 (WFPC2) aboard the *Hubble Space Telescope.* A detailed description of the WFPC2 can be found in *HST* WFPC2 Instrument Handbook, Version2.0 (Burrows et al. 1995). The nucleus of the galaxy was centered on the Planetary Camera chip (PC1), which has a pixel size of 0."046, corresponding to 6.7 pc at the distance of NGC 4261 (30 Mpc), and a field of view of 36″ × 36″ (=5.2 × 5.2 kpc). The gain and readout noise are $7e^-$/DN and $7e^-$, respectively. All observations were obtained with the telescope guiding in fine lock, which has a nominal pointing stability of about 3 mas.

Since a narrowband filter covering the wavelength region of the redshifted Hα + [N II] emission (~6500–6700 Å) is not available for WFPC2, we used the wide-band filter F675W (transformed to Cousins *R*) for the on-band observations. Two off-band images were obtained in emission free spectral regions on either side of the Hα emission using the filters F547M (~Johnson *V*) and F791W (~Cousins *I*). The exposure times were 2000 s for the on-band image, and 800 s for each off-band image. All exposures were divided into two equally long images, referred to as CR-split frames, to facilitate cosmic-ray removal.

HST data are routinely calibrated using a standard pipeline maintained by the Space Telescope Science Institute (STScI). The reduction steps are performed in the following order: correction of small A/D errors; subtraction of a bias level for each chip; subtraction of a superbias frame; subtraction of a dark frame; correction for shutter shading effects and division by a flat field. The reduction procedure is described in detail by Holtzman et al. (1995).

As mentioned previously, two CR-split frames were obtained for each filter. The alignment of the two frames in each CR-split pair was checked by using the position of the 20 brightest globular clusters present in the PC1 field of view. In all cases the two images were registered to better than 0.05 pixels and could therefore be combined without further processing. In the combining process, cosmic rays were flagged by comparing the difference in counts between pairs of corresponding pixels to a local sigma calculated from the combined effects of Poisson statistic and read-out noise. If the difference was higher than 3 times the expected sigma, the value for that pixel in the output image was replaced by the lowest of the two input values.

Unlike the case of frames belonging to the same CR-split pair, images taken with different filters are not perfectly aligned. As for the CR-split pairs, the alignment of the F547M, F675W, and F791W images was calculated by using the position of 20 globular clusters imaged in the PC1. The off-band images are shifted by as much as 1.7 pixels with respect to the on-band images and were therefore aligned to the on-band image before proceeding.

The raw counts have been transformed to *V*, *R*, and *I* magnitudes following the guidelines given by Holtzman et al. (1996). The equations that transform counts to *V*, *R*, and *I* magnitudes include $V-R$ and $V-I$ color terms. The final magnitudes have been calculated by first approximating the $V-R$ and $V-I$ color terms involved in the photometric transformations with $(m_{\rm F547M}-m_{\rm F675W})$ and $(m_{\rm F547M}-m_{\rm F791W})$, respectively, where $m_{\rm filter}=-2.5\log DN+m_0$, DN is the count rate measured in that particular filter, and m_0 is the photometric zero point tabulated for each filter by Holtzman et al. (1996), and then iterating the process until convergence. The accuracy of the photometric zero points is about 0.1 mag.

2.2. *FOS Observations*

Spectra of NGC 4261 were obtained on 1995 August 3 using the *HST* Faint Object Spectrograph (FOS). A description of the instrument can be found in the FOS Instrument Handbook (Keyes et al. 1995). One of the 0."1 PAIR square apertures (projected dimensions on the sky 0."09 × 0."09) was used to measure the spectrum of the nuclear dust disk at the 13 positions shown in Figure 2. In the remainder of this paper we will refer to the different aperture positions as labeled in the figure. The nucleus was acquired through a multiple-stage peak-up (Keyes et al. 1995). Subsequent analysis of the grid formed by the peak-up's steps and dwells, showed that the nucleus was centered to within one-fifth of the aperture size, or 20 mas. The center of each aperture position was calculated using *HST*/Fine Guidance Sensors engineering telemetry after the observations were completed. The relative accuracy of the aperture centers is 3 mas.

The grating used, G570H, covers the wavelength region between 4570 and 6870 Å, has a dispersion of 4.36 Å per diode, and a spectral resolution of 4.01 Å, as determined from the FWHM of several emission lines measured in wavelength calibration spectra taken immediately before and after the observing sequence. The spectra are quarter-stepped, a procedure in which the spectrum is stepped onto the linear array of 512 diodes by one-quarter of the diode width along the dispersion direction. The final spectrum is therefore composed by 512 × 4 pixels sampled at 1.1 Å intervals. The exposure times were 2040 s at all positions, except for the NE off-axis position, which was exposed for 1640 s, the SE and NUC positions, which were both exposed for 2030 s.

The spectra were calibrated using the standard pipeline procedure described by Keyes et al. (1995). In order to obtain higher accuracy in the wavelength scale than allowed by the standard calibration, two wavelength calibration spectra were obtained immediately before and after the observing sequence. The wavelength zero point derived from the two calibration spectra agree to within 20 km s^{-1}, which therefore defines the accuracy of our wavelength scale.

At the time this paper is written, inverse sensitivity curves are not available for the 0."1 aperture, therefore flux calibration is not performed as part of the standard procedure. In order to convert count rates to fluxes (in ergs cm^{-2} s^{-1} $Å^{-1}$) we used the inverse sensitivity curve for the 4."3 FOS aperture, multiplied by the relative throughput of the 0."1 versus the 4."3 aperture. The error on the resulting absolute fluxes may be as large as 50%, because the relative throughput, which is measured only for pointlike sources, is strongly dependent on the centering of the source in the 0."1 aperture. However, relative fluxes should be correct to within a few percent; furthermore, the arguments put forward in § 4 are based entirely on the central velocity and velocity dispersion of the emission lines, and are independent on the accuracy of the absolute flux calibration.

3. IMAGING ANALYSIS AND RESULTS

3.1. *Morphology*

The fully reduced *V*, *R*, and *I* *HST*/WFPC2 images of NGC 4261 are shown in Figure 1 (Plate 3). The scale and orientation is the same in the three images, but the intensity level has been adjusted independently for each, so that relative brightness cannot be inferred from the figure. In the WFPC2 *R* image, which includes the Hα + [N II] complex, a bright region of line emission surrounds the nucleus. The continuum emission from the nucleus, presumably of nonthermal origin, is itself unresolved in the *V* and *I* images. The *V*, *R* (after subtracting line emission as described in § 3.4) and *I* magnitudes of the nucleus are 22.6 ± 0.15 mag, 21.9 ± 0.22 mag, and 21.3 ± 0.15 mag, respectively, uncorrected for extinction. The large errors are due to uncertainties in estimating the background in the region surrounding the nucleus; for the *R* magnitude, we added the additional uncertainty associated with the subtraction of the line emission.

However, the most striking feature unveiled by the WFPC2 images is the nuclear dust disk, approximately 1."6 × 0."7 (=230 × 100 pc). Dust in the central region of NGC 4261 was first detected by Kormendy & Stauffer (1987) thanks to unsharp masking techniques, but the disk was first recognized as such by Jaffe et al. (1993) using WFPC1 images taken before the 1994 December servicing mission that corrected for the spherical aberration affecting the *HST* primary mirror. Jaffe et al. (1993) argue that if a massive black hole is responsible for the nuclear activity in AGNs, the dust disk may act as an "outer accretion disk,"

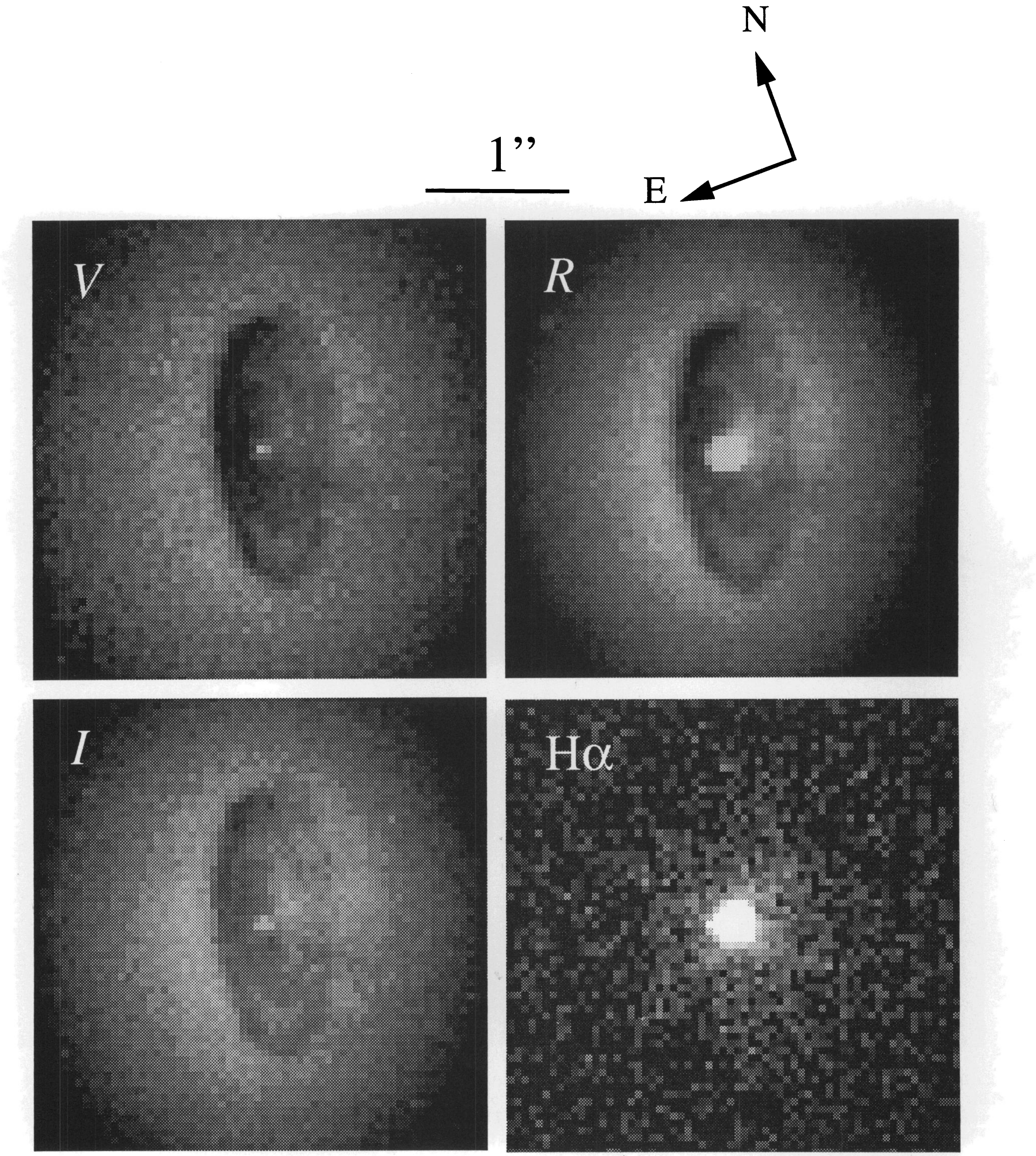

FIG. 1.—*HST*/WFPC2 *V*, *R*, and *I* images of NGC 4261. The galaxy was centered in the PC. Only the inner ~3″ are shown. The *V* and *I* off-band images are shown in the left panels, while the *R* on band image and the continuum-subtracted Hα images are shown in the panels to the right. The scale and orientation, shown at the top, are the same for the four images.

FERRARESE, FORD, & JAFFE (see 470, 446)

by supplying fuel to the central engine. On the basis of the fact that the disk is nearly perpendicular to the galaxy radio jet, The authors propose that the disk is responsible for the orientation of the jets, possibly through the transfer of angular momentum from the disk to the central black hole. The restored resolution capabilities of the WFPC2 allow a more detailed study of the structure of the dust disk than was possible in Jaffe et al. (1993, 1996) using WFPC1 data. In the remainder of this section we will perform a complete analysis of the disk's morphology, stressing the connection between the disk and the central engine.

By looking at Figure 1, a few observations can be readily made. From the ratio of minor to major axis, we estimate that the normal to the disk forms a 64° angle with the line of sight. However, the disk is not perfectly elliptical in shape; a small protuberance is seen extending from the north edge; in addition, the north side of the ellipse is rounder and wider than the south side, possibly suggesting that the disk is slightly warped or twisted along its major axis. In § 4.2, we will show, from independent spectroscopic data, that the innermost part of the disk is not coaxial with the outer part, confirming that the disk is warped. The disk is not homogeneous; several bright filaments, reminiscent of spiral structure, can be detected extending from the nucleus to the north and south sides of the disk. These patterns repeat identically in the three photometric bands and cannot be attributed to line emission from ionized gas (see § 3.4); comparison of the broadband colors with the predictions of single burst stellar population models (Bruzual & Charlot 1993; Leitherer & Heckman 1995) shows that no significant star formation is present in the disk, and therefore the filaments most likely correspond to regions with lower dust content, and therefore lower optical depth than the surroundings.

The spiral structure may provide the means by which angular momentum is transferred from the center of the disk out, allowing the innermost material to sink toward the center. In § 4.1, we will present evidence for large random motions and shock waves in the innermost parts of the disk, both of which could be produced by the gravitational energy released by the gas infalling into the black hole potential well.

Further evidence that the disk is not in an equilibrium configuration comes from noticing that the major axis of the disk, with a position angle of 163° ± 2°, is misaligned with respect to the major axis of the galaxy, at a position angle of 158°.5 ± 0°.4 (§ 3.2). While a misalignment in the projected major axes of the disk and of the galaxy could correspond to an equilibrium configuration if the galaxy was triaxial, the intrinsic figure of NGC 4261 is most likely a prolate spheroid, with no or very little trace of triaxiality (Davies & Birkinshaw 1986). As noted by Jaffe et al. (1996), the axis of the radio jets, 88° ± 1° (Birkinshaw & Davies 1985) projects about 15° from the minor axis of the disk, implying that the jets and the disk are not exactly perpendicular to each other. Finally, a linear dust feature is seen extending beyond the southwest edge of the disk in a radial direction, at a position angle of ~220°, or about 33° from the minor axis of the dust disk. A similar, but much fainter feature extends in the opposite direction, beyond the northeast edge of the disk, suggesting that we may be looking at a linear jet of dust ejected from the nucleus (a dust ring or disk seen edge on would produce the same optical depth on both sides of the nucleus, contrary to the observations). The radio jet and the presumed dust jet are roughly, although not exactly, perpendicular to the disk: in agreement with Jaffe et al. (1993), we identify the east side of the disk (which appears darker by virtue of the fact that the line of sight through it encounters fewer unobscured stars) with the near side. Simple geometrical arguments predict that the near side of a feature perpendicular to the disk will project onto the far side of the disk, corresponding to the darker, west side. In fact, Birkinshaw & Davies (1985) show that the radio jet projecting to the west is the brightest, and is therefore probably approaching us by virtue of Doppler boosting effects. Also the near side of the dust feature, which we identify with the darker jet, projects to the west. These observations suggest a strong causal relationship between the disk and the radio activity, as speculated by Jaffe et al. (1993, 1996), even if the connection between the dust jet and the radio jet is unclear: the angle between the two is about 48°, therefore if gas and dust had been dragged away from the disk in the direction of the jet, then we would have to conclude that the jet is precessing. The effects of such a large precession would be evident as a distortion in the radio lobes, which is not observed: the radio jets are straight with an opening angle of less than 1'.5 out to 4' from the nucleus (Birkinshaw & Davies 1985). However, at the present time the processes that accelerate radio jets are not completely understood, and the possibility that the jet could accelerate cooler material at some angle to the jet axis cannot be excluded.

Jaffe et al. (1996) noted that the disk is not positioned at the isophotal center of the galaxy and found marginal evidence that the nucleus itself is not at the center of either the disk or the galaxy. We repeat the analysis using the higher resolution images presented in this paper. We define the position of the center of the galaxy as the mean of the centers of the isophotes between 1".9 and 4" (see § 3.2 for a description of the isophotal fitting algorithm); in this range the isophotes are not perturbed by the central dust disk, and the isophotal center is very stable: the rms error of the average position of the center is less than 3 mas in both right ascension and declination. The position of the center of the galaxy coincides in the three images to within 2 mas. The position of the nucleus was measured both by PSF fitting and by Gaussian centroid. Both methods give consistent results. Because of the non homogeneous background in the disk, the position of the nucleus is uncertain by ~9 mas. In the *R* images, the position of the nucleus was measured after subtracting the Hα emission as described in § 3.4. Within the errors, the position of the nucleus is the same in the three images. The same can be said for the center of the dust disk, which is defined as the center of the ellipse that best fits the edge of the disk. Because the disk is not perfectly elliptical, the position of the center suffers a large uncertainty, one PC pixel, or 46 mas. The orientation and position of the centers of the isophotes, the dust disk and the nucleus are summarized in Table 1. The *x*- and *y*-coordinates on the WFPC chip are transformed to right ascension and declination using the pointing information provided by the STScI. The right ascension and declination can suffer from a systematic zero point error due to uncertainties in the guide stars positions (which could amount to 1"–1".5 for NGC 4261, which is located close to the edge of the Sky Survey plate), to focal plane calibration errors (up to 0".6), and to internal refraction in the WFPC2 filters (up to 0".2, an effect referred to as filter wedge). Taking these

TABLE 1

NGC 4261 ASTROMETRY

Parameter	R.A. (J2000)	Decl. (J2000)	P.A. (degrees)	Ellipticity
V isophotes	12 19 23.2204 ± 0.0002	5 49 30.775 ± 0.003	158.5 ± 0.4	0.25 ± 0.02
R isophotes	12 19 23.2203 ± 0.0002	5 49 30.774 ± 0.003	158.5 ± 0.4	0.25 ± 0.002
I isophotes	12 19 23.2200 ± 0.0002	5 49 30.773 ± 0.003	158.5 ± 0.4	0.25 ± 0.02
Nucleus V	12 19 23.2183 ± 0.0006	5 49 30.776 ± 0.009	N/A	N/A
Nucleus R	12 19 23.2189 ± 0.0006	5 49 30.768 ± 0.009	N/A	N/A
Nucleus I	12 19 23.2188 ± 0.0006	5 49 30.766 ± 0.009	N/A	N/A
Outer Disk V	12 19 23.2146 ± 0.003	5 49 30.753 ± 0.05	163. ± 2	0.54 ± 0.08
Outer Disk R	12 19 23.2146 ± 0.003	5 49 30.753 ± 0.05	163. ± 2	0.54 ± 0.08
Outer Disk I	12 19 23.2146 ± 0.003	5 49 30.753 ± 0.05	163. ± 2	0.54 ± 0.08
Inner Disk	12 19 23.22 ± 0.03	5 49 30.44 ± 0.5	199. ± 7	0.6 ± 0.1
Radio Emission......	12 19 23.18 ± 0.01	5 49 29.5 ± 0.2	88. ± 1	N/A

NOTES.—In addition to the formal errors reported in the table, the right ascension (in hours, minutes, and seconds) and declination (in degrees, arcminutes and arcseconds) for the isophotal center, the nucleus and the center of the dust disk can suffer from a systematic zero point error of 1.″5–2″. The position of the radio nucleus was measured by Chris O'Dea, Joseph Lehar, & Huub Röttgering using the VLA at 10 GHz in the A-array. The position angle of the radio jet is from Birkinshaw & Davies (1985).

errors into account, the positions listed in Table 1 coincide with the ones derived by Jaffe et al. (1996). They also agree with the position of the radio nucleus, measured by Chris O'Dea, Joseph Lehar, and Huub Röttgering using the VLA at 10 GHz in the A-array. The position angle of the radio jet reported in Table 1 is from Birkinshaw & Davies (1985).

The center of the galaxy, the nucleus, and the center of the disk do *not* coincide. The offset of one with respect to the other is the same in the three color bands. With respect to the center of the galaxy, the nucleus is shifted by 23 ± 9 mas (= 3.3 ± 1.3 pc) to the southwest, while the disk is shifted by 90 ± 46 mas (= 13 ± 7 pc) in the same direction. A schematic representation of these results is given in Figure 2 (Plate 4), showing an enlarged section of the V-band image. The ellipse best representing the edge of the dust disk and the best fitting elliptical isophote just outside the disk are drawn in blue and white, respectively; the miscentering and different orientation of the two is readily apparent. The miscentering between the nucleus and the isophotal center, which amounts to less than half a pixel, is less evident but statistically significant, while the offset between the disk and the nuncleus is quite abvious. The displacement of the disk with respect to the center of the galaxy may suggest that the dust has an external origin and has not yet reached equilibrium. This hypothesis, already advanced by Jaffe et al. (1996), is further supported by the fact that the disk spin axis, which projects approximately along the minor axis of the galaxy, is different from the galaxy spin axis (the galaxy rotates around its major axis; Davies & Birkinshaw 1986). This could be the case if the dust had been captured from a cannibalized galaxy, rather than being accreted from material internal to NGC 4261 itself. However, Hau & Thomson (1994) show that a near collision with another galaxy can have the result of spinning the envelope in a direction different from the intrinsic nuclear spin direction. In this hypothesis, an external origin for the dust is not required.

Could the nucleus, and the associated black hole, have been acquired in a recent capture of a nearby galaxy? The decay time for oscillations of a point source with mass M in the gravitational potential of a stellar system with radius $R_{\rm core}$ and mass $M_{\rm core} \gg M$, is approximately $t_{\rm cross} M_{\rm core}/M$ where $t_{\rm cross}$ is the crossing time of the stars in the core, moving with a velocity $V_{\rm stars}$: $t_{\rm cross} = R_{\rm core}/V_{\rm stars}$. For $R_{\rm core} = 1.''83 = 260$ pc (this is the value of $r_{0,1}$ from § 4.2), we find $M_{\rm core} = 2.5 \times 10^9$ $M_\odot$ (see § 4.2). Assuming $M = 5 \times 10^8$ $M_\odot$ (§ 4.2) and $V_{\rm stars} = 100$ km s^{-1}, we find that the decay time is of the order of 10^7 years. Therefore, it seems improbable that we would have caught this nucleus within only 10 million years of its capture, and we therefore argue against a recent capture.

We note that the nucleus is displaced along the direction of the radio jet. It is highly suggestive to think of the displacement of the nucleus with respect to the center of the galaxy as due to a recoil produced by the radio jets. In this hypothesis, supposing that a jet with total radio luminosity L is collimated and pushing against a nucleus of mass M in the same direction for a time t, then the nucleus will be displaced by $\Delta d = (0.5Lt^2)/(Mv\eta)$, where v is the velocity of the jet, and η is the ratio of radio luminosity to total kinetic luminosity. For NGC 4261 the total radio luminosity is $L = 3.6 \times 10^{41}$ ergs s^{-1} (see § 3.4). An upper limit to the time t can be estimated by noting that the jets are about 4′ long, or 35 kpc, and assuming that the jet is moving with $v = 0.1c$, we obtain $t \leq 35$ kpc/$0.1c \leq 10^6$ yr. For $M = 5 \times 10^8$ $M_\odot$ (see § 4.2), we have $\Delta d \sim 0.003/(v\eta)$ pc. Since typical values of v in low-luminosity radio sources like NGC 4261 are $0.1c$ to $0.3c$, whille a reasonable estimate for the kinetic efficiency is $\eta = 0.01$–0.1, recoil from the radio jet can move the nucleus by a few parcsecs, and therefore account for the observed displacement. The idea that nuclei could be displaced by recoil from the radio jets was already advanced by Rudnick & Edgar (1984) and Shklovsky (1982).

3.2. *Isophotal Analysis and Surface Brightness*

The isophotal parameters, ellipticity, position angle of the major axis, deviation of the isophotes from pure ellipses [defined by the fourth-order cos (4α) Fourier coeficient; e.g., Peletier 1990] and surface brightness, as a function of the distance from the center, were determined using an iterative method described by Jedrzejewski (1987) and implemented in the IRAF task ELLIPSE. Figure 3 shows the V brightness profile and the $V-I$ and $V-R$ color profiles, obtained by simply subtracting the calibrated surface brightness at the same radius in two different color bands, the colors are therefore integrated along the galaxy isophotes. This procedure is possible since the ellipticity, position angle, and

1996ApJ...470..444F

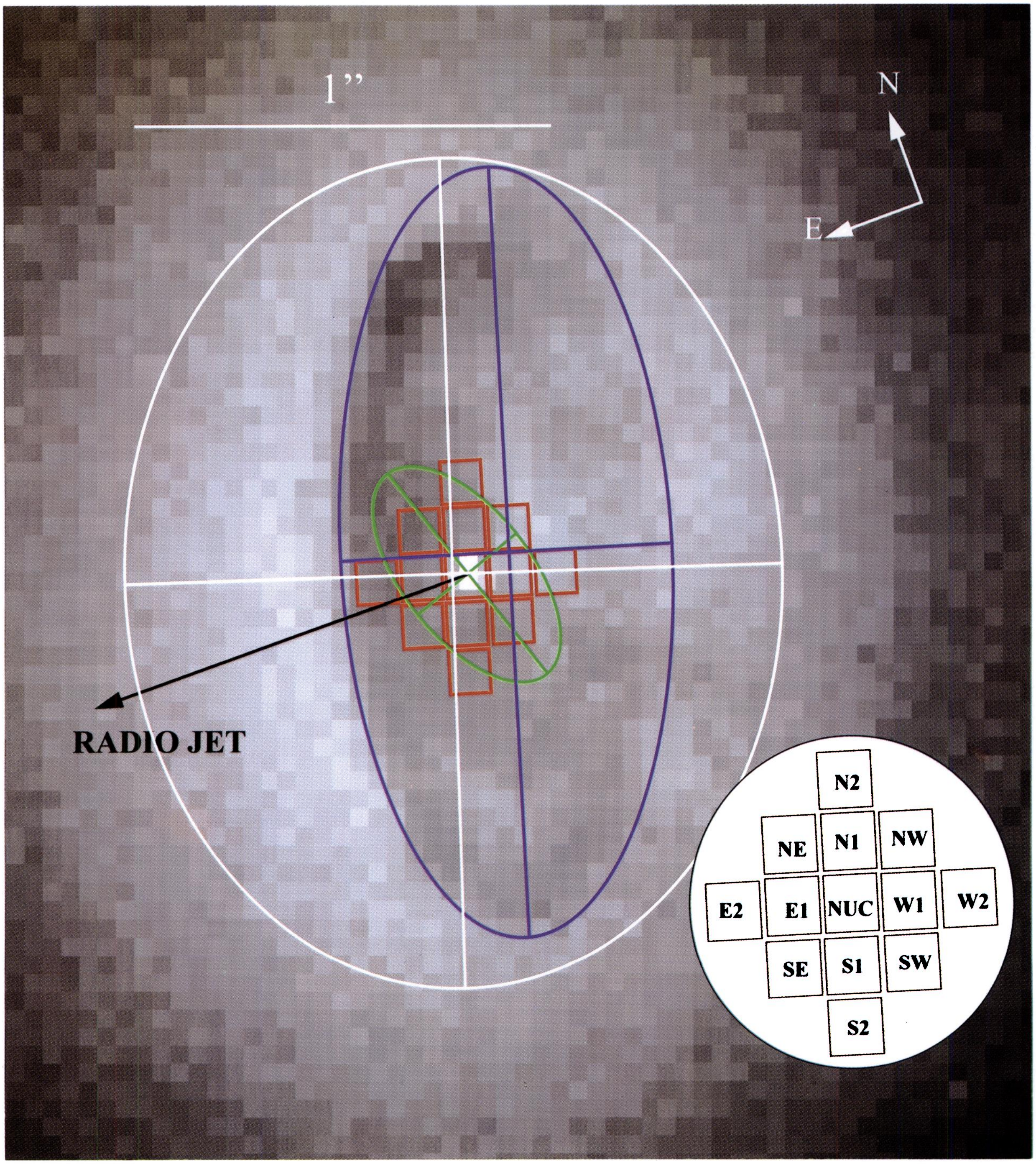

FIG. 2.—An enlarged view of the nuclear dust disk, obtained from the V-band image (*upper left panel of Fig. 1*). Superimposed onto the image is the ellipse that best fits the edge of the disk (*in blue*) (§ 3.1), and the elliptical isophote just outside the disk (*in white*) (§ 3.2). As can be seen, the center of the disk does not coincide with the isophotal center of the galaxy, the offset being 90 ± 46 mas. The nucleus is also offset with respect to the isophotal center by 23 ± 9 mas to the west. The red squares represent the position of the 13 *HST*/FOS aperture pointing, named as indicated in the inset in the lower right. The green ellipse shows the best disk model that reproduces the velocity map obtained from *HST*/FOS spectra (§ 4.2).

FERRARESE, FORD, & JAFFE (see 470, 448)

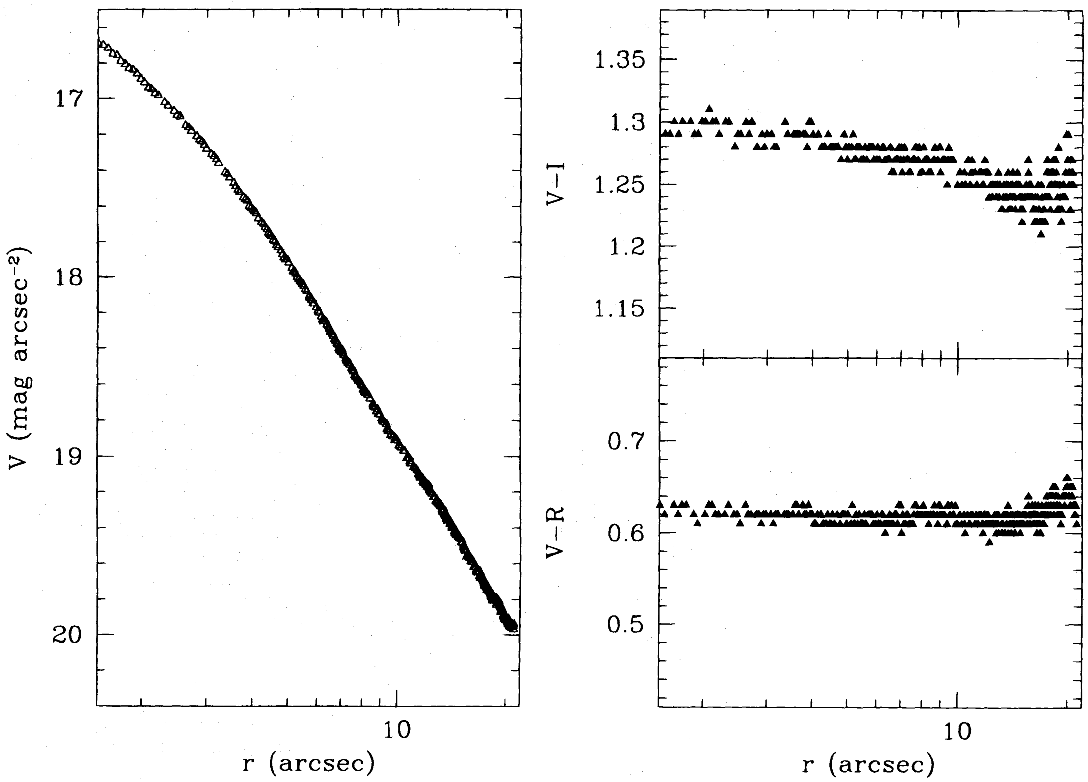

FIG. 3.—The V brightness profile and the $V-I$ and $V-R$ color profiles as a function of the semimajor axis length

Fourier coefficients for the galaxy are virtually identical in the three filters. The brightness profiles rise steeply to the center of the galaxy, with no sign of a corelike flattening, although there is a slight change of slope at $r \sim 3\farcs5$. The colors in the main body of the galaxy are those of a coeval stellar population with a nominal age between 13 and 20 Gyr (Bruzual & Charlot 1993; Leitherer & Heckman 1995).

The ellipticity, the major axis position angle, the fourth-order cosine Fourier coefficient, and the position of the isophotal center as a function of the semimajor axis length are shown in Figure 4, in V, R, and I. The V-band isophotal parameters are in perfect agreement with the results obtained by Ferrarese et al. (1994) and van den Bosch et al. (1994) from *HST*/WFPC1 images.

Ellipticity, major axis position angle, and Fourier coefficients do not show any dependence on color at any of the radii observed here, a result that was also found by Peletier et al. (1990) using B, J, and K images. The negative cos (4α) Fourier coefficient indicates that the isophotes are boxy compared to the best-fitting ellipse, a condition that is shared by a large percentage of radio-loud and X-ray–emitting ellipticals (Bender et al. 1989). Boxy isophotes may be caused by high orbital angular momentum stars from an infalling secondary (May, van Albeda, & Norman 1985), supporting the hypothesis that NGC 4261 has undergone a merging process and that the disk has an external origin. Boxiness in the isophotes was discovered from ground-based observations by Lauer (1985), Mollenhoff & Bender (1987), and Peletier (1990), and was confirmed again by van den Bosch et al. (1994) from *HST* images. Around 15″–20″, the isophotes tend to be not as boxy as for smaller radii, and in fact at 20″ the cos (4α) Fourier coefficient is zero, i.e., the isophotes are almost perfectly elliptical. The ellipticity decreases at radii larger than 10″ and increases slightly again between 15″ and 20″. The position angle remains constant over the entire range of observed radii.

The derived isophotal centers show a very interesting behavior as a function of semimajor axis length. In Figure 4, the zero points of the right ascension and declination coincide with the coordinates of the isophotal center reported in Table 1. Both right ascension and declination are very stable up to 10″ from the center, but then the isophote centers start shifting significantly. At approximately 20″ from the center, the isophotes are shifted by $\sim 0\farcs2$ (~ 5 pixels) to the north, and $\sim 0\farcs1$ (~ 2 pixels) to the west. This trend repeats identically in the three photometric bands. Since globular clusters were masked in the isophotal fitting procedure, they cannot be spuriously distorting the isophotes. The only instrumental effect we are aware of that could give rise to a gradient in the PC chip, and therefore affect the result of the isophotal analysis, is the so called "charge transfer effect" (Holtzman et al. 1995). At the CCD operating temperature of -88°, Holtzman et al. (1995) measure a 3%–4% peak to peak gradient in the photometry across each chip due to charge transfer inefficiencies, in the sense that a star appears fainter at higher row numbers (= higher y coordinate in the PC1). In our case, if anything, this effect should produce an artificially lower background mainly toward the north and only slightly toward the west, with the result that the isophotal center at large radii should be artificially shifted toward the south and, in a much smaller way, toward the east, exactly opposite to the observed shift. We conclude that the measured shift of the isophotal center with radius is *real* i.e., intrinsic to NGC 4261 itself. In Figure 4 the solid line in the right ascension versus r and declination versus r plots represents the position of the nucleus relative to the isophotal center defined in Table 1, while the dotted line represents the position of

1996ApJ...470..444F

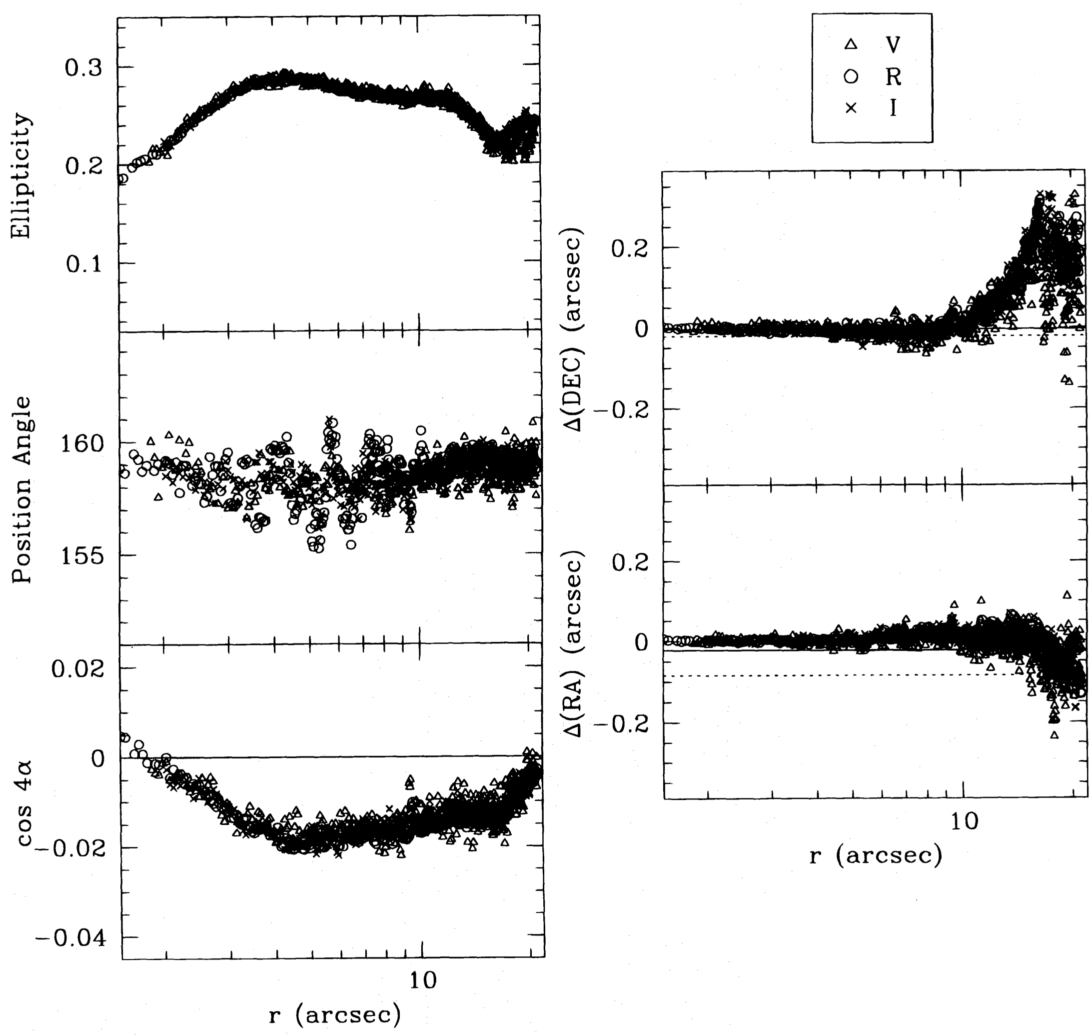

FIG. 4.—The ellipticity, the position angle of the isophotes major axis, the fourth-order cosine Fourier coefficient, and the position of the isopotal center in V, R, and I as a function of the semimajor axis length.

the center of the disk. In right ascension, both nucleus and disk are shifted, with respect to the isophotal center (defined as the mean between 1″.9 and 4″) mainly to the west, i.e., in the same direction as the isophotes at large radii (> 10″). The shift of both nucleus and disk in declination is much smaller, and in fact consistent with no shift at all within the quoted errors (Table 1). The change in the isophotal center at large (> 10″) radii could be the result of a tidal disturbance. If this is the case, we can derive a timescale for the interaction by noting that while the outer parts of the galaxy are still distorted, the center of the galaxy has apparently relaxed. The relaxation time will be a few times the radius at which the transition occurs (10″ = 1.4 kpc) divided by the stellar orbital velocity, ~100 km s^{-1}. This is 10^7–10^8 yr. Finally, we note that off-centered isophotes are not uncommon in ellipticals: in a sample of 45 nearby ellipticals, Lauer et al. (1995) found seven cases of galaxies with nonconcentric isophotes, two of which contain dust.

3.3. *Optical Depth and Reddening in the Nuclear Dust Disk*

In contrast with Jaffe et al. (1996), who derived an optical depth for the dust by assuming a function for the underlying brightness distribution, we can construct an optical depth map of the disk by using the color information provided by the two V and I images. We adopted the extinction law by Cardelli, Clayton, & Mathis (1989) and assumed $R_V = A(V)/E(B-V) = 3.1$, the standard value for the diffuse interstellar medium. As shown by Cardelli et al. (1989) for the filters used, the final solution for the optical depth is not very sensitive to the value adopted for R_V: if $R_V = 5$, as measured in some dense clouds, the derived optical depth would increase by about 20%. As a first approximation, we assume that the disk lies in the plane of the sky and crosses the center of the galaxy, so that it dims the light from only half of the stars along the line of sight. Furthermore, we assume that the $V-R$ and $V-I$ colors are constant inside the disk and equal to the value measured in the region immediately surrounding it: $V-I = 1.29$ and $V-R = 0.62$.

Figure 5 (Plate 5) shows a gray-scale image of the optical depth map in the disk. Brighter areas correspond to higher opacities. The linear dust feature protruding from the southwest side of the disk is clearly visible. The optical depth varies between about one on the western side of the disk, to about two at the eastern side. The change in optical depth in the direction parallel to the minor axis of the disk is most likely an artifact due to neglecting the inclination of the disk in deriving the reddening: since the normal to the disk forms an angle of about 64° with the line of sight, the

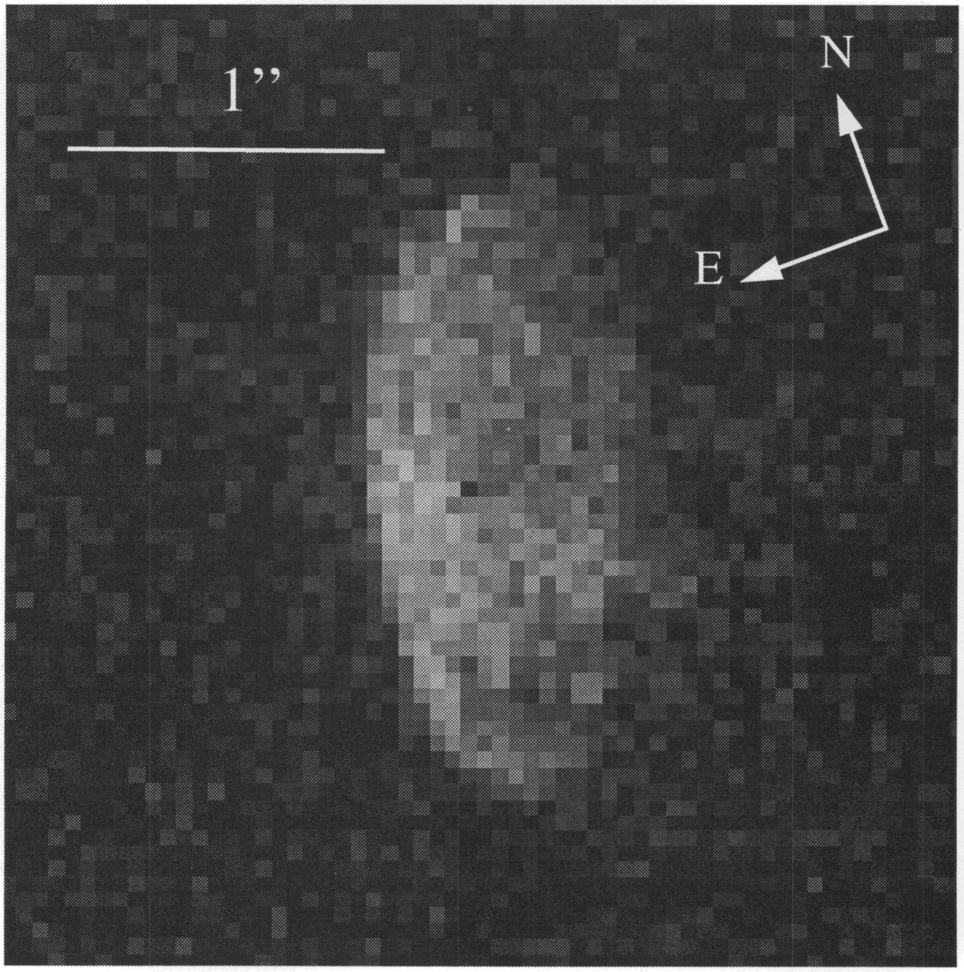

FIG. 5.—A gray-scale image of the optical depth map in the disk. The area shown is 3″ × 3″, and the orientation of the image is as in Fig. 1. Brighter areas correspond to higher opacities.

FERRARESE, FORD, & JAFFE (see 470, 450)

1996ApJ...470..444F

line of sight to the near side will pass through fewer unobstructed stars than the line of sight to the far side, which will therefore appear brighter than the near side. If this effect is neglected in modeling the reddening, because of the wavelength dependence of the extinction, the far (brighter) side will appear to have a lower optical depth than the near side. The optical depth map can be used to construct dust-free V, R, and I images. Figure 6 compares cuts across the minor and major axis for the original and the de-extincted images in all three photometric bands. The brightness profile of the deextincted images is a smooth function of radius, which gives us confidence in the good quality of the optical depth map.

The knowledge of the optical depth can be used to estimate the total mass of neutral and molecular hydrogen in the disk. Using the value of the Galactic ratio of the surface density of hydrogen (atomic plus molecular form) to the color excess $E(B-V)$ by Bohlin, Savage, & Drake (1978), we find that the mass of the neutral and molecular hydrogen in the disk is $(5.4 \pm 1.8) \times 10^4 \, M_\odot$, which is negligible compared to the mass of the underlying stellar population, $\sim 2 \times 10^9 \, M_\odot$ (see § 4.2). The value of the disk mass derived in this paper is consistent with the findings of Jaffe et al. (1993), which further note that the total mass in the disk, if converted into energy at 1%–2% efficiency, corresponds to the total energy in the radio lobes, about 10^{57} ergs, assuming a synchrotron lifetime of $\sim 10^8$ yr.

3.4. *Structure and Properties of the* Hα *Emission*

In order to produce a pure line-emission image, the two deextincted V and I off-band images were averaged, and the resulting image, scaled by an appropriate factor, was subtracted from the deextincted on-band R image. The scaling factor is determined by the requirement that the subtracted image has zero net counts in the region between 3″ and 6″ from the center, where no emission is expected.

The resulting continuum subtracted emission line image is shown in the lower right panel of Figure 1. The line emission is concentrated in a circular region around the nucleus and decreases rapidly with increasing distance from the center. There is no indication of structure in the emitting region. Subtraction of a theoretical point spread function

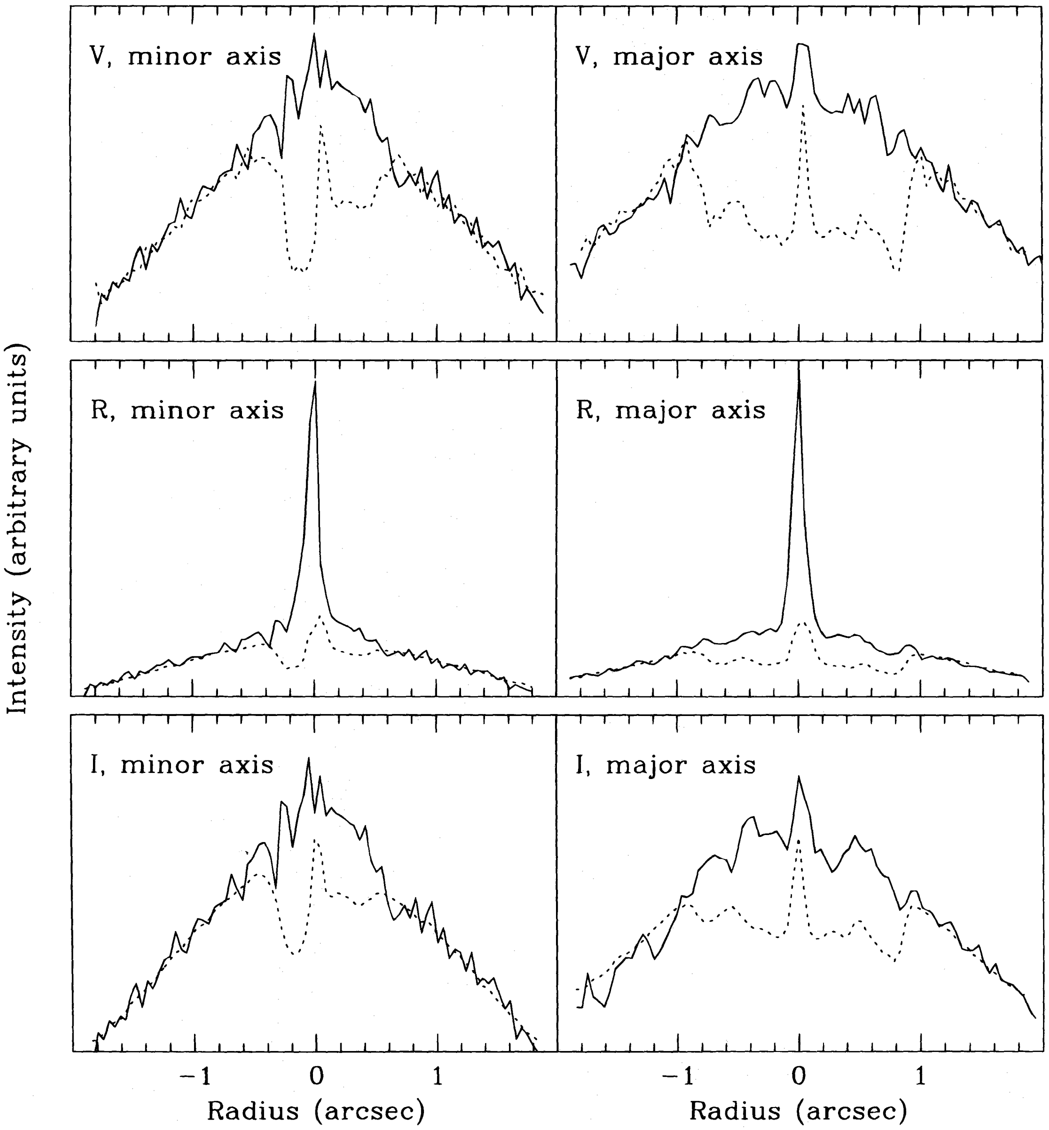

FIG. 6.—Cuts across the minor and major axis for the original (reddened; *dashed line*) and the unreddened (*solid line*) images in all three photometric bands. The zero point of the x-axis is at the position of the nucleus.

(PSF), created using the TinyTIM software (Krist 1995), shows that the emission is resolved: the FWHM of the *HST*/PC1 PSF is of the order of 1.46 pixels, or 0".07, while the FWHM of the emission region is 2.64 pixels, or 0".12. Figure 7 shows a cut through the center of the line-emitting region along the minor axis of the dust disk (in fact, the surface brightness of the line emission is the same along any axis through the center), superimposed to a cut through a PC PSF, scaled so that its maximum coincides with the maximum in the line emission. The PSF is obvously narrower than the emitting region. The wings of the emitting region can be reproduced assuming an exponential surface brightness of the type $I(r) = I_0 \times 10^{-r/r_0}$, where $I(r)$ is the line flux as a function of the distance from the center r. However, a simple model of this type, while able to fit the wings of the line emitting region, cannot fit the core at the same time, and the additional contribution of a central point source is needed. The bottom panel of Figure 7 shows the residuals obtained by subtracting from the profile of the line emitting region, a model produced by adding a point source with central power $\sim 1.9 \times 10^{-12}$ ergs cm^{-2} s^{-1} arcsec^{-1} to a disk with surface brightness $I = 1.8 \times 10^{-12} \times 10^{-r/0.2''}$ ergs cm^{-2} s^{-1} arcsec^{-1}.

The *R* filter transmits [O I] λλ6300, 6364, [N II] λλ6548, 6583, Hα, and [S II] λλ6717, 6731. In order to derive the Hα luminosity, we adopted as the ratio of the fluxes of the [O I] doublets to the flux in the [N II] + Hα complex the values derived from the FOS nuclear spectra presented in § 4 and Table 2. The FOS spectral resolution is not sufficient to resolve the [N II] + Hα complex; in addition, the [S II] fluxes are unreliable since the doublet falls on the red edge of the spectral range. Therefore, we derived the ratio of the fluxes of the [N II] and [S II] doublets to the Hα flux from the high-resolution ground-based spectra presented by Jaffe et al. (1996). Under these assumptions, the Hα flux was estimated from the continuum subtracted image shown in Figure 1 using the photometric calibration derived by Holtzman et al. (1996, formula 11). The resulting Hα flux is $F(\mathrm{H}\alpha) = 1.4 \times 10^{-13}$ ergs cm^{-2} s^{-1}. Assuming a distance to NGC 4261 of 30 Mpc, the total Hα luminosity is $L(\mathrm{H}\alpha) = 1.5 \times 10^{40}$ ergs s^{-1}.

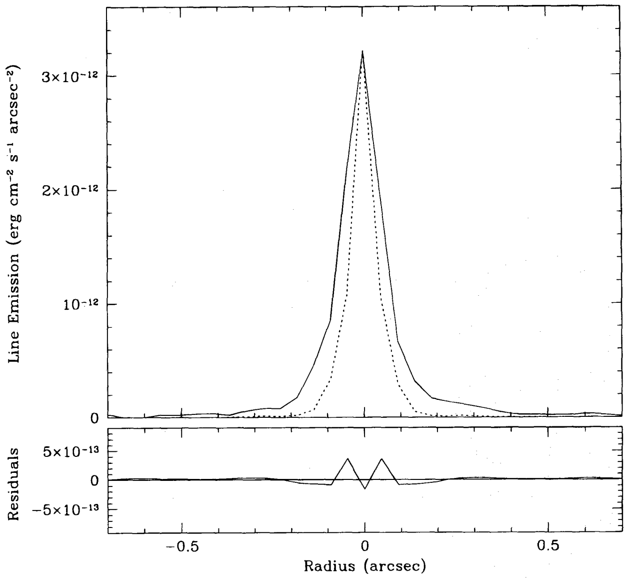

FIG. 7.—*Top panel*: the solid line shows a cut through the center of the line-emitting region along the minor axis of the dust disk, while the dotted line shows a cut through a PC PSF, arbitrarily scaled. *Bottom panel*: residuals obtained by subtracting from the profile of the line emitting region, a model obtained by adding a point source with central power $\sim 1.9 \times 10^{-12}$ ergs cm^{-2} s^{-1} arcsec^{-2} to a disk with surface brightness $I = 1.8 \times 10^{-12} \times 10^{-r/0.2''}$ ergs cm^{-2} s^{-1} arcsec^{-2}.

Is the Hα luminosity of NGC 4261 typical of AGNs with similar X-ray and radio fluxes? Using a sample of strong radio sources, Baum & Heckman (1989) found that a very good linear relation exists between the logarithms of the total Hα + [N II] line luminosity L_{line} and of the total radio luminosity from the entire radio source L_{radio}, in the range $10^{40} < L_{\mathrm{radio}} < 10^{46}$: $\log L_{\mathrm{line}} = (0.73 \pm 0.06) \log L_{\mathrm{radio}} + (10 \pm 2.5)$. The emission-line luminosity of NGC 4261 is $L_{\mathrm{line}} = 4.9 \times 10^{40}$ ergs s^{-1}, assuming [N II]/Hα = 2.3 from Jaffe et al. (1996); while the total radio luminosity can be calculated assuming a spectral index of −0.6 (estimated from the radio fluxes at 21 and 6 cm given by Roberts et al. 1991) and integrating the resulting flux between 10^7 and 10^{11} Hz (following the prescription of Baum & Heckman 1989). The result, for a distance to NGC 4261 of 30 Mpc, is $L_{\mathrm{radio}} = 3.6 \times 10^{41}$ ergs s^{-1}. Therefore, the line emission and radio luminosity lie very nicely on the Baum & Heckman relation.

Trinchieri & di Serego Alighieri (1991) found from a sample of 13 galaxies with extended X-ray emission that Hα emission is often associated with the presence of very hot gas. This is true for NGC 4261, for which a luminosity of 1.0×10^{40} ergs s^{-1} is detected in the energy band between 0.5 and 4.5 keV (Roberts et al. 1991, assuming a distance of 30 Mpc). However, the Hα luminosity in NGC 4261 is at least a factor 10^4 higher than expected from the recombination of the cooling X-ray gas, which is estimated to be 10^{34} to 10^{36} ergs s^{-1} (Trinchieri & di Serego Alighieri 1991), implying that an additional source of ionization is required. In the simplest scenario, this can be provided by photoionization by the active nucleus (Baum & Heckman 1989), a hypothesis that can be tested easily by comparing the number of ionizing nonthermal UV photons emitted by the nuclear source with the number of ionizing photons necessary to produce the observed Hα emission. In case B recombination (i.e., the gas is optically thick to Lyman photons but optically thin to Balmer photons), The number of photons with energy larger than 13.6 eV required to explain the observed Hα flux has to be greater than $N = 7.34 \times 10^{11} \times L(\mathrm{H}\alpha) = 1.1 \times 10^{52}$ photons s^{-1} (Osterbrock 1989). The number of ionizing photons emitted from the central source, estimated from the nuclear continuum flux observed by Jaffe et al. (1996), assuming that the flux, per unit frequency interval, behaves as $F_\nu = F_0 \nu^{-1}$ and that there is no cutoff at high frequencies, is in fact of the right order of magnitude: $\sim 10^{52}$ photons s^{-1}. We note that, even if photoionization by the active nucleus is an important source of ionization, other sources of ionization are certainly active. For example, shocks may be a source of excitation: the spectra discussed in § 4 show faint traces of [O I] λ6300 and [N I] λ5200, which have very low ionization potential and are therefore interpreted as shock tracers.

From the knowledge of the electron density N_c and the total Hα luminosity $L(\mathrm{H}\alpha)$, it is straightforward to estimate the volume filling factor f (Osterbrock 1989).

$$n_e^2 = \frac{L(\mathrm{H}\alpha)}{f V \alpha^{\mathrm{eff}}_{\mathrm{H}\alpha} h\nu_{\mathrm{H}\alpha}}, \qquad (1)$$

TABLE 2

NGC 4261 EMISSION-LINE PROPERTIES

Aperture Position	Ion	Line Flux	Mean LOS Velocity (km s^{-1})	FWHM (km s^{-1})
NUC......	Hβ	32 ± 5	226 ± 204	2104 ± 473
NUC......	[O III] λ4960	50	2274	2082
NUC......	[O III] λ5008	149 ± 14	2274 ± 72	2082 ± 142
NUC......	[O I] λ6302	149	1994	2014
NUC......	[O I] λ6366	487 ± 41	1994 ± 94	2014 ± 191
NUC......	[N II] λ6548	189	2078	1497
NUC......	[N II] λ6583	581 ± 14	2078 ± 36	1497 ± 75
NUC......	Hα	311	2078	2500 ± 216
NUC......	[S II] λ6719	24	1912	899
NUC......	[S II] λ6733	91 ± 2	1912 ± 85	899 ± 159
N1	Hβ	<14	2386 ± 247	<2000
N1	[O III] λ4960	7	2310	800
N1	[O III] λ5008	20 ± 3	2310 ± 120	800 ± 200
N1	[N II] λ6548	41	2329	630
N1	[N II] λ6583	122 ± 14	2329 ± 46	630 ± 100
N1	Hα	66	2329	732 ± 100
N1	[S II] λ6719	28	2037	900
N1	[S II] λ6733	84 ± 14	2037 ± 89	900 ± 200
N2	[N II] λ6548	3	2128	300
N2	[N II] λ6583	8 ± 3	2128 ± 91	300 ± 150
N2	Hα	<7	2128	<1500
S1	[N II] λ6548	9	1887	<500
S1	[N II] λ6583	28 ± 7	1887 ± 91	<500
S1	Hα	<21	1887	<1500
W1	[O III] λ4960	18	2050	1200
W1	[O III] λ5008	48 ± 11	2050 ± 120	1200 ± 200
W1	[N II] 6548	59	1996	700
W1	[N II] λ6583	182 ± 14	1996 ± 68	700 ± 100
W1	Hα	76	1996	825 ± 200
W1	[S II] λ6719	14	1858	800
W1	[S II] λ6733	55 ± 7	1858 ± 134	800 ± 200
W2	[N II] λ6548	6	2087	350
W2	[N II] λ6583	17 ± 2	2087 ± 137	350 ± 200
W2	Hα	<14	2087	
E1	[N II] λ6548	13	2060	850
E1	[N II] λ6583	38 ± 3	2060 ± 137	850 ± 150
E1	Hα	21	2060	1000 ± 500
NW	[N II] λ6548	15	2233	500
NW	[N II] λ6583	48 ± 7	2233 ± 46	500 ± 100
NW	Hα	27	2233	1000 ± 300
NE	[N II] λ6548	14	2338	600
NE	[N II] λ6583	42 ± 14	2338 ± 46	600 ± 200
NE	Hα	22	2338	870 ± 435
SW	[N II] λ6548	14	1827	615 ± 200
SW	[N II] λ6583	41 ± 11	1827 ± 46	615 ± 150
SW	Hα	22	1827	747 ± 421

NOTES.—Line fluxes are in units of 10^{-15} ergs cm^{-2} s^{-1} arcsec^{-2}.

where V is the volume occupied by the gas, $\alpha_{\mathrm{H}\alpha}^{\mathrm{eff}} = 1.17 \times 10^{-13}$ cm^3 s^{-1}, h is Plank's constant and $\nu_{\mathrm{H}\alpha}$ is the frequency of the Hα line. For simplicity, we assume that the gas is uniformly distributed in a sphere 0ʺ.12 in diameter (corresponding to the FWHM of the observed line emitting region). The electron density was estimated by Jaffe et al. (1996) to be $\sim 3 \times 10^4$ cm^{-3}. Plugging in all the numbers, we find that the volume filling factor is $f = 5 \times 10^{-4}$. This value depends on the geometry of the emitting region and is most likely a lower estimate: for example, if the ionized gas is distributed in a thin disk, rather than in a sphere, the filling factor would in fact be an order of magnitude higher than the value quoted.

The mass of the ionized gas, obtained following Osterbrock (1989) is $M_{\mathrm{gas}} = f\,V(n_p m_p + N_{\mathrm{He}} m_{\mathrm{He}})$, where n_p, m_p and n_{He}, m_{He} are the densities and masses for hydrogen and helium, respectively. Assuming $n_{\mathrm{He}} = 0.1 n_p$ and $n_e = n_p + 1.5 n_{\mathrm{He}}$, we find that the mass of the gas ranges between a few tens to a few hundreds solar masses, depending on the geometry of the emitting region.

4. SPECTROSCOPIC ANALYSIS AND RESULTS

In this section, we present the *HST*/FOS spectra obtained in the nuclear region of NGC 4261 at 13 different aperture positions. As a first step in our analysis, we fitted the spectra using a line synthesis program and derived velocity centroids, line width and fluxes for all the emission lines detected at the different aperture positions (§ 4.1). In § 4.2, we discuss the results and derive an estimate for the central mass and mass-to-light ratio.

4.1. *Spectral Analysis*

The spectra of NGC 4261 obtained at locations E2, S2, and SE (see Fig. 2) do not have enough S/N to allow detection of any emission lines. In Figures 8*a* and 8*b* are shown the spectra obtained at the remaining 10 aperture positions, in the wavelength regions between 4900 and 5200 Å, and between 6200 and 6850 Å, where emission lines are detected.

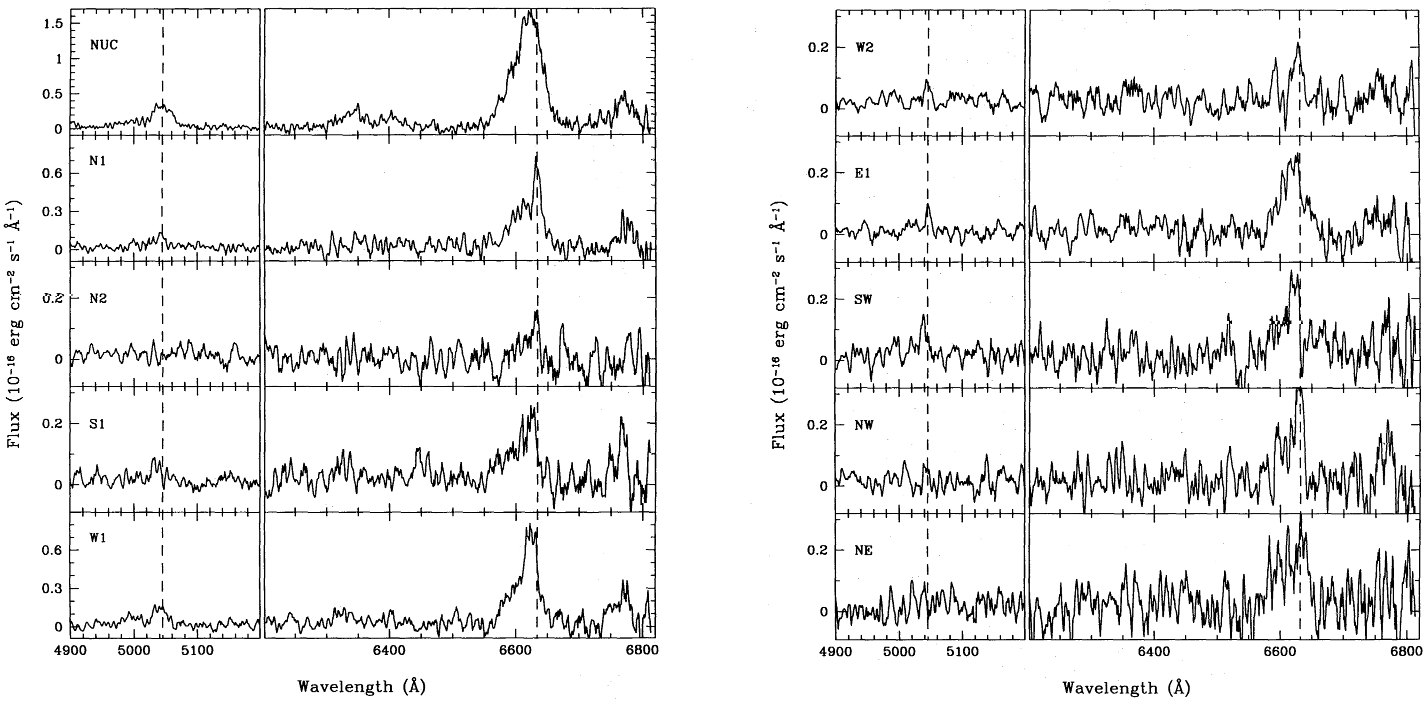

FIG. 8*a*

FIG. 8*b*

FIG. 8.—(*a*) The spectra obtained in the wavelength regions between 4900 and 5200 Å, and between 6200 and 6850 Å, for five of the 10 aperture positions at which emission lines are detected. The dashed lines represent the systemic velocity expected for the [O III] λ5007 and [N II] λ6584 emission. (*b*) The spectra obtained in the wavelength regions between 4900 and 5200 Å, and between 6200 and 6850 Å, for five of the 10 aperture positions at which emission lines are detected. The dashed lines represent the systemic velocity expected for the [O III] λ5007 and [N II] λ6584 emission.

The dashed lines represent the systemic velocity expected for the [O III] λ5007 and [N II] λ6584 emission. The complete spectrum obtained at the nuclear position (NUC; see Fig. 2) is shown in the upper panel of Figure 9 (Plate 6). Emission lines of Hα Hβ, [O III] λλ4459, 5007, [O I] λλ6300, 6364, [N II] λλ6548, 6584, and [S II] λλ6717, 6731 are prominent. All the emission lines appear unusually broad: line fitting, described in the following paragraph, shows a FWHM of ~1500 km s^{-1}. Because of the drastic decrease in the line flux with increasing distance from the nucleus, observed in the Hα WFPC2 image, The S/N in the off-nuclear spectra decreases dramatically, and only the strongest emission lines can be detected. The lower panel of Figure 9 overplots the [N II] + Hα spectral region at positions NUC, N1, and S1, i.e., along the major axis of the dust disk. The fluxes at the off-nuclear positions have been scaled to facilitate the comparison. The solid vertical line is at the systemic velocity of the galaxy, 2210 ± 14 km s^{-1} (de Vaucouleurs et al. 1991). This velocity agrees well with other values reported in the literature (Huchra et al. 1983; Davies & Birkinshaw 1986). The dashed lines show the centroids of [N II] λ6584 at the three aperture positions. The spectra show the clear signature of rotation; the N1 emission is redshifted with respect to the systemic velocity, while both the NUC and S1 position are blueshifted. The blueshift of the NUC emission is most likely due to a small offset between the aperture position and the nucleus.

A more detailed analysis is performed by finding the central velocities, line fluxes, and full widths at half-maximum for each line. This was done by using the line synthesis program SPECFIT (Kriss 1994). First of all, the continuum was fitted with a cubic spline, constrained in the regions not contaminated by line emission, using standard IRAF routines. Subsequently, SPECFIT simultaneously fits the continuum plus a user specified number of emission lines with Gaussian profiles. The fit was performed by constraining the ratios of the central wavelengths and line strengths of each pair of a doublet ([O III], [O I], [N II], and [S II]) to standard values (Osterbrock 1989). In addition, because of the relative low spectral resolution of our data, the Hα + [N II] complex is not fully resolved, and in order to constrain the fit, we fixed the redshift of the Hα emission to be the same as that of the [N II] lines. Unfortunately, because of the low S/N of the spectra at all locations other than the nuclear one, in the N1 and W1 spectra we are able to detect only the [O III], [S II], and Hα + [N II] lines, while at all other off-nuclear positions, only the Hα + [N II] complex can be accurately measured. The spectra at locations E2, S2, and SE do not have enough S/N to allow detection of any emission lines. None of the spectra provides enough S/N to allow measurement of stellar absorption lines. Figure 10 shows the result of the line fitting for the Hα + [N II] complex at three aperture positions.

A digression is necessary at this point. The *HST* PSF at the position of the FOS aperture overfills the 0".1 aperture, therefore, nuclear light from the PSF wings will contaminate the off-nuclear spectra. Unfortunately, good measurement or models of the PSF are not available, however, at first order, the PSF at the FOS position is similar to the PSF at the PC1 position. This last PSF is known in detail and can therefore be used to roughly estimate the amount of contamination. Based on the shape of the PC1 PSF, a 0".09 aperture centered 0".09 away from the center of the PSF (this is the case of the N1, S1, W1, and E1 aperture positions) "sees" 12% of the light that fills a 0".09 aperture perfectly centered. The same aperture centered 0".18 from

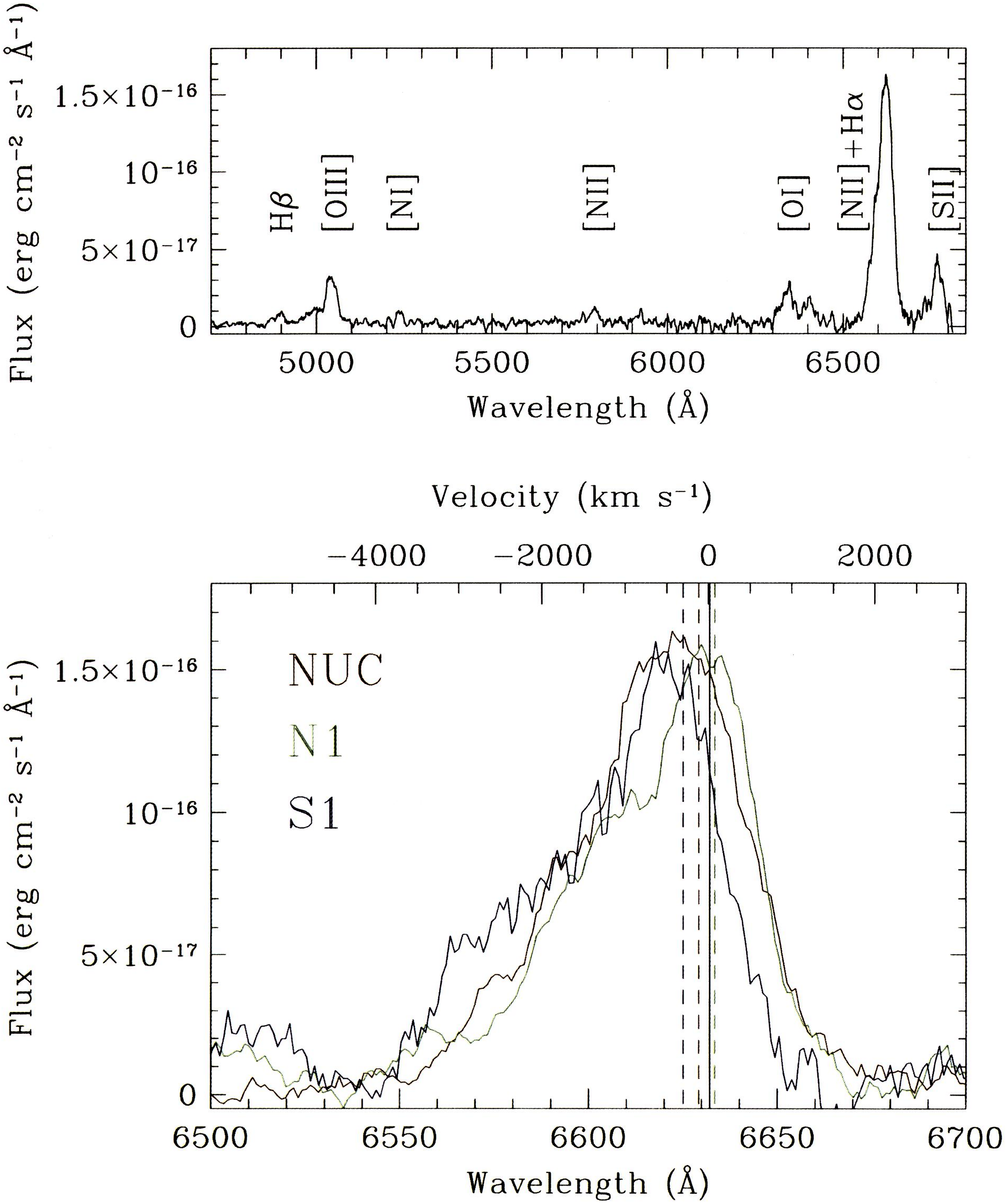

FIG. 9.—The upper panel shows the spectrum of NGC 4261 obtained at the nuclear position. The lower panel overplots the [N II] + Hα spectral region at positions NUC, N1, and S1, i.e., along the major axis of the dust disk. The fluxes at the off-nuclear positions have been scaled to facilitate the comparison. The vertical line marks the position of the [N II] λ6584 emission at the systemic velocity of the galaxy, 2210 ± 14 km s^{-1} (de Vaucouleurs et al. 1991), while the three vertical dashed lines mark the centroid of the [N II] λ6584 emission at the three different aperture positions.

FERRARESE, FORD, & JAFFE (see 470, 454)

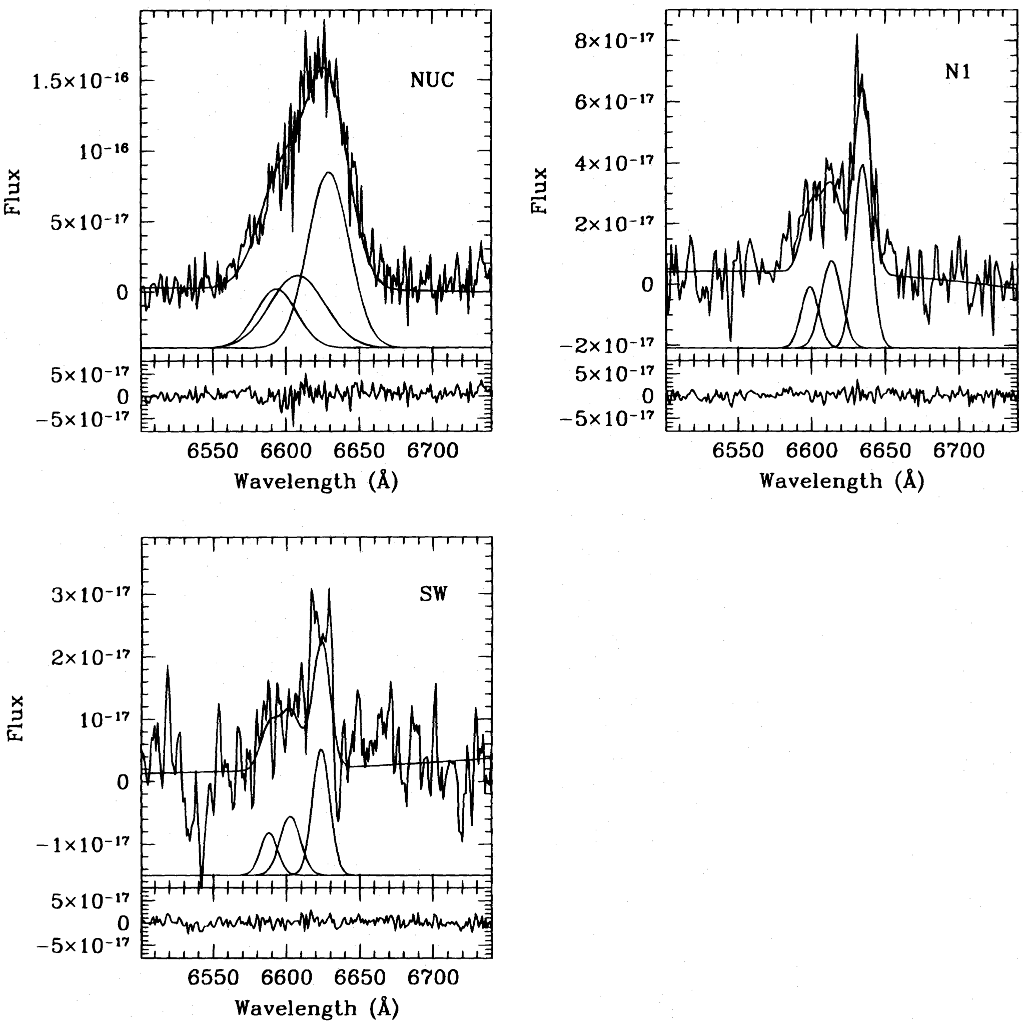

FIG. 10.—The result of the line fitting for the Hα + [N II] complex at three aperture positions, NUC, N1, and SW. The units of flux are ergs cm^{-2} s^{-1} Å^{-1}. The solid line overplotted on the spectra represents the best fit. The single Gaussian components are also shown. The residuals from the fit are shown in the lower panels.

the PSF center (i.e., W2, E2, N2, and S2 aperture positions) is contaminated by only 0.7% of the nuclear light, while a 0."09 aperture 0."13 from the center (NW, SW, NE, and SE aperture positions) is contaminated by 2% of the nuclear light. Thus, ideally, before fitting each off-nuclear spectrum we should subtract the contribution of the light scattered to that position from the nucleus. However, the numbers quoted are correct only for a point source. Furthermore, they vary by as much as 50% depending on where the source is centered within the aperture. Indeed, the nuclear spectrum, scaled by the above-mentioned factors is incompatible with several of the off-nuclear spectra: for example, at position S1, the predicted flux scattered from the off-nuclear spectrum in the [N II] lines is larger the flux *measured* in the lines, and it does not reproduce the observed line profile (FWHM and central velocity). How much in error are the estimates of flux, central velocity, and line width if the nuclear contamination is neglected? We answered this question by fitting line profiles to the spectra taken at positions N1 and W1 (these are the spectra with the highest S/N ratios) first by neglecting nuclear contamination and then assuming that 12% of the nuclear light is scattered into the two apertures (for the reasons mentioned above this is likely to be an upper limit to the amount of scattered light). We found that, while the line flux can be overestimated by at most a factor of 2 if the scattered light is neglected, errors on the central wavelength and FWHM are small compared to internal uncertainties on the same quantities. This is due to the fact that, as will be shown in Table 2, the FWHM of the emission lines decreases rapidly from the center outward: the FWHM of the [N II] lines in the nuclear spectrum is ~1500 km s^{-1}, while the FWHM of the same lines 0."09 and 0."18 away from the nucleus decreases to about 600 and 300 km s^{-1}, respectively. Therefore, at each off-nuclear position the emission lines comprise a broad component scattered from the nucleus plus a much narrower and therefore more strongly peaked component from the ionized gas in the aperture. Since the fit is more strongly affected by the line peaks (which have higher S/N ratio) than by the line bases, central velocities, and FWHM are not strongly affected by the scattered light. This result, established for the apertures adjacent the nucleus, is even more strongly valid for the apertures farther away, since the ratio of the fluxes measured at each aperture position to the fluxes scattered from the nucleus increases with distance from the center (see Table 2). Therefore, since all of the conclusions in § 4.2 depend on central velocities and line width, rather than on line fluxes, in the following discussion, rather than adopting clumsy and incorrect estimates of the scattered light, we neglect nuclear contamination altogether. As a consequence, the line fluxes derived from the fit should be considered as upper limits to the real fluxes.

Table 2 lists the central velocities, line strengths, and FWHM for all fitted lines at each aperture position. The line strengths agree well with the fluxes measured from the WFPC2 Hα image in 0''.09 square areas reproducing the positions of the FOS apertures, confirming that the FOS and PC1 PSFs are similar, as assumed in the previous paragraph. From the table, it is immediately apparent that at the three aperture positions at which the centroids of the [O III], [N II], and [S II] lines can be measured, the [O III] lines seem to be redshifted with respect to the Hα + [N II] complex, while the [S II] lines are blueshifted. Once the errors are taken into account, the shifts are significant only at the NUC position. The origin of this discrepancy is not clear at this time. As explained in § 3.2, wavelength calibration was performed using two lamp spectra taken immediately before and after the observing sequence. No variation in the line positions is seen in the two spectra, indicating that the wavelength scale was stable during the observations. In addition, the wavelength dispersion derived from the lamp spectra agrees with the standard value adopted for the FOS, making it unlikely that a scale error is present in the data. It is possible that the [O III], [S II], and [N II] lines arise from different regions within the nucleus, and therefore the shifts are inherent to the data. In all events, the conclusions put forward in the remainder of this paper, will not be affected. Those conclusions are based entirely on the relative shifts of the [N II] lines at different aperture positions: even admitting a systematic scale error in the wavelength scale, the stability of wavelength scale during the observations implies that the central wavelengths of the same line at different aperture positions have a relative accuracy of a few km s^{-1}.

Several other points are worth mentioning and will be discussed in detail in the following sections. First of all, the central velocity of the [N II] lines in the nuclear spectrum is 2078 ± 36 km s^{-1}, slightly lower than the systemic velocity (2210 ± 14 km s^{-1}; de Vaucouleurs et al. 1991). This value is also lower than the value quoted by Jaffe et al. (1996) for the [N II] emission in their nuclear spectrum. The source of this discrepancy is unknown at this time; however, we note that the determination of the central mass carried on in § 4.2 depends only on the velocity differences observed at different aperture positions, i.e., at different distances from the center, and does not depend on the absolute zero point of the velocity scale. The most striking result is the change in the central velocity of the emission lines with distance from the center. The most dramatic change is present for the two positions imediately north and south of the nucleus, along the major axis of the nuclear dust disk: the emission at position S1 is blueshifted relative to the emission at the NUC position by 191 ± 98 km s^{-1}, while the emission at position N1 is redshifted by 251 ± 58 km s^{-1}. The errors quoted are the formal rms errors calculated by the line synthesis program used to fit the spectra. On the other hand, the velocities along the minor axis of the dust disk (W1, W2, E1), do not show such extreme variation. The velocity pattern along the major and minor axis of the disk therefore suggests that the gas is approximately in circular motion. The velocities derived from the off-axis spectra suffer large uncertainties due to the low S/N of the data, but fit the general picture of the gas being roughly in circular motion. An additional clue to the gas dynamics in the nuclear region is given by the very clear tendency for the lines FWHM to decrease with distance from the center: the FWHM of the [N II] lines at the nuclear position is about 1500 km s^{-1}, and decreases to 500 km s^{-1} 0''.09 away from the nucleus, and ~350 km s^{-1} 0''.18 away. The large line width at the nuclear position and the absence of obvious asymmetries in the line profiles suggest that the lines are broadened by rotation and/or turbulence. The symmetry of the higher signal-to-noise ratio line profiles in the Jaffe et al. (1996) data lead to the same conclusion.

The observations argue against the case of a gas outflow: a one-directional outflow would give rise to asymmetric line profiles, which are not observed. A bidirectional outflow roughly perpendicular to the dust disk would produce the largest velocity shift along the minor, rather than the major axis, contrary to the observations. In addition, an outflow is not compatible with the [N II] + Hα morphology, derived both from the spectra and from the WFPC2 images: no changes in the emission fluxes are observed as a function of the polar angle, as would be expected is the ionized gas has a bipolar distribution.

Before proceeding, we would like to address one concern arising from the possibility that the central velocities may be systematically shifted due to partial obscuration of the ionized gas. However, partial obscuration would sensibly affect the line profiles, in addition to the central velocity, since the side of the line coming from material more heavily obscured would be suppressed. Since such asymmetries are not found in either our or in the Jaffe et al. (1996) data, we can exclude the possibility that the partial obscuration, if present at all, has a significant effect on the central velocities.

4.2. *Determination of the Central Mass*

As pointed out in § 1, NGC 4261 is a *strong* candidate in the search for a nuclear black hole. Large velocity changes are seen along the major axis of the disk, and the large width of the forbidden lines at the nuclear position fitted very nicely in the "black hole picture." In particular, the large velocity difference observed for the gas 0''.09 away from the nucleus along the major axis of the dust disk ($\Delta v = 442 \pm 100$ km s^{-1} between the N1 and S1 positions), if ascribed entirely to circular motion of the ionized material in the plane of the disk, points to a total mass inside $r =$ 0''.09 of $M = r(\Delta v/2)^2/[G \sin^2(i)] \sim 1.8 \times 10^8 M_\odot$, where G is the gravitational constant and i is the angle between the normal to the disk and the line of sight (=64°; see § 3.1). At the end of this section, we will show that the total V luminosity integrated in a sphere 0''.09 in radius, is $2.3 \times 10^5 L_\odot$, and therefore the stellar mass inside the same volume is at least 3 orders of magnitude lower than the central mass estimated from the velocity measurements. Of course, our reasoning depends entirely on the assumption that the gas is in circular motion. In the remainder of this section we will validate this hypothesis by showing that the velocity map from the 10 aperture positions in which the [N II] emission lines could be measured is consistent with the prediction of a simple model in which the gas is in Kelperian rotation. The final mass we derive from the entire data set is larger than the rough estimate calculated above, because the kinematic line of nodes of the inner disk of ionized gas differs from the geometrical major axis of the dust disk.

1996ApJ...470..444F

Following the procedure outlined by Harms et al. (1994), we compared the observed velocities to the prediction of a simple model in which the gas is confined in a disk in Keplerian motion around a central mass. The model depends on three parameters: the central mass $M_{\rm BH}$ (which plays the role of a simple scaling factor), the angle i between the normal to the disk and the line of sight, and the angle θ between the projected major axis of the disk and the line connecting the N1 and S1 exposures.

The predicted radial velocity as a function of distance from the center r is given by Harms et al. (1994). In comparing the model with the observed velocities, three more parameters come into play: the systemic velocity of the galaxy (i.e., the zero point of the velocity map), and the offsets Δx and Δy, in both x- and y-directions, that could have occurred between the center of the FOS nuclear exposure and the center of the Hα emission due to an imperfect peak-up. We allowed for the offset between the central exposure and the nucleus by sampling r, in the model, every $0''.0181$, or one-fifth of the distance between the centers of adjacent aperture positions. The model was first run for 1° increments of both θ and i and for $(GM_{\rm BH})^{1/2} = 1$. This allowed us to find the values of θ, i, Δx, and Δy for which the sum of the square of the differences between observed and predicted velocities is minimized. The data are best fitted by assuming that in the region sampled by the FOS exposures the gas is confined in a disk whose normal forms a $\sim 69°$ angle with the line of sight, and with major axis position angle $\sim 199°$. The inclination of 69° derived from the kinematic data is in good agreement with the geometrical inclination of the dust disk, 64°. Errors on both ellipticity and position angle are of the order of 20%. According to the best fit, the center of the ionized gas disk is shifted with respect to the position at which the NUC spectrum was taken by $0''.02$ ($\frac{1}{5}$ of an aperture size) along the minor axis of the disk to the west, and by the same amount along the major axis to the north. The geometrical properties of the Keplerian disk, which are measured on a much smaller scale than the one defined by the outer dust disk, are summarized in Table 1, under the lavel "inner disk." The absolute positions of the center of the inner disk are determined from the pointing information provided by the FOS exposure. Figure 11 shows a plot of the predicted velocities versus the observed velocities for the best fitting model. The predicted velocities, derived from the model for $(GM_{\rm BH})^{1/2} = 1$, are in units of arcsec$^{-1/2}$. The data is very well fitted by a straight line, implying that the assumption that the gas is in Keplerian motion is correct. The intercept of this line with the y-axis defines the systemic velocity v_s of the galaxy, while the slope of the line is equal to $(GM_{\rm BH})^{1/2}$. A weighted least-square fit to the data yields $v_s = 2124 \pm 40$ km s^{-1}, which is lower than the RC3 value (2210 ± 14 km s^{-1}), and $M_{\rm BH} = (4.9 \pm 1.0) \times 10^8\ M_\odot$ for a distance to NGC 4261 of 30 Mpc.

The spectroscopic observations support the hypothesis, already advanced from the study of the morphology of the dust disk (§ 3.1), that the gas and dust are not in an equilibrium configuration. The inner disk, defined by the spectroscopic data, is rotated toward the east by $\sim 36°$ with respect to the outer dust disk observed from the WFPC2 images, suggesting that the entire structure is tilted and warped. Jaffe et al. (1996), in their analysis of the morphology of the dust disk in relation to the radio morphology, note that the minor axis of the dust disk and the axis of the radio jet are not perfectly aligned (the difference in the two position angles is 15°). The hypothesis that the disk aligns the radio jet by determining the inclination and angular momentum of the accretion disk does not leave space for such a discrepancy. However, the FOS observations show that the inner parts of the disk are twisted with respect to the outer parts, and the twist is in the sense of bringing the minor axis of the disk toward the projected axis of the radio jet. This means that the orientation of the inner accretion disk, which in turn determines the direction of the radio jet, most likely does not coincide with the orientation of the outer dust disk.

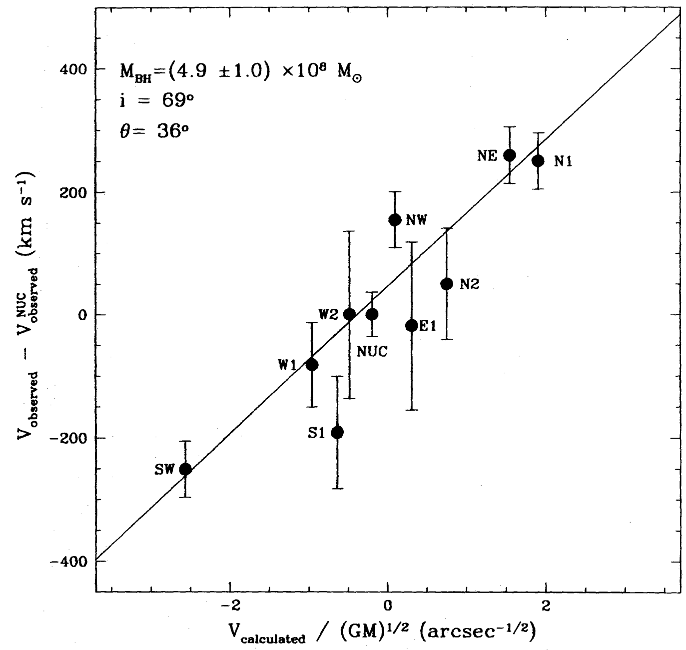

FIG. 11.—Predicted velocities vs. the observed velocities for the best-fitting Keplerian model. The data can be fitted by a straight line, implying that the gas is in Keplerian motion. The predicted velocities, derived from the model for $(GM_{\rm BH})^{1/2} = 1$, are in units of arcsec$^{-1/2}$.

Before proceeding, we need to discuss one possible caveat. The model presented in the previous paragraph does not take into account the contribution of the stellar potential and the disk potential to the velocity field. The mass of the disk was calculated in § 3.3 to be $(5.4 \pm 1.8) \times 10^4\ M_\odot$, which is not large enough to affect the velocities in any important way. Even adding to this the mass of the ionized gas calculated from the Hα flux (§ 3.4) does not change the result. The predicted rotational velocity along the major axis of the disk due to a disk with total mass $6 \times 10^4\ M_\odot$ and constant mass density is shown as a dashed line in Figure 12. The gravitational potential due to stars was calculated by first fitting the unreddened V brightness profile (§ 3.3) with the sum of two exponentials:

$$I(r) = I_{0,1} \times e^{(-r/r_{0,1})} + I_{0,2} \times e^{(-r/r_{0,2})}\ , \qquad (2)$$

and then deprojecting the observed brightness to derive a luminosity density, which, for an exponential brightness profile, and in the assumption of spherical symmetry, is proportional to a K_0 Bessel function.

The best fit to the unreddened V brightness profile yields:

$$\begin{aligned} I_{0,1} &= 3.08 \times 10^8\ L_\odot\ \text{arcsec}^{-2} \\ &= 1.4 \times 10^4\ L_\odot\ \text{pc}^{-2}\ , \quad r_{0,1} = 1''.83\ ; \qquad (3) \end{aligned}$$

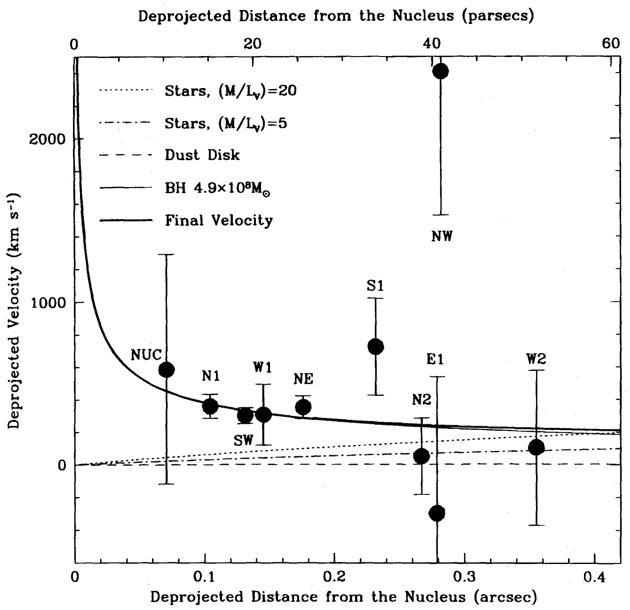

FIG. 12.—The dashed, dash-dotted, and dotted solid lines show the expected rotation curve due to the nuclear dust disk (assuming a mass of 6×10^4 $M_\odot$ and constant mass density), the stars (for $(M/L)_V = 5$ and under the conditions described in § 4.2), and the stars again but for $(M/L)_V = 20$. The thin solid line shows the rotation curve due to a 4.9×10^8 $M_\odot$ black hole. The thick solid line shows the final velocity taking into account the black hole, the disk and the stars [for $(M/L)_V = 5$]. The data points, corrected for the projection effects using the best fitting models described in § 4.2, are superimposed to the figure. Because of the small centering error in the FOS peakup discussed in the text, the velocity of the nucleus is plotted as a data point. With respect to Fig. 11, multiplication by the projection factor amplifies the error bars.

$$I_{0,2} = 6.4 \times 10^7\ L_\odot\ \mathrm{arcsec}^{-2} = 3.0 \times 10^3\ L_\odot\ \mathrm{pc}^{-2}\ ,$$
$$r_{0,2} = 8''.73\ , \qquad (4)$$

A double exponential was also used in fitting the V-reddened brightness profile of NGC 4261 by Jaffe et al. (1996), giving consistent results (note that Jaffe et al. [1996] assumed that NGC 4261 is in the Virgo cluster, and therefore at half the distance adopted in the present paper. This has to be taken into account when comparing Jaffe et al. results with ours).

The contributions to the orbital velocity due to the stars, assuming mass-to-light ratios $(M/L)_V = 5$ and $(M/L)_V = 20$, are shown in Figure 12 as dot-dashed and dotted lines, respectively, as a function of distance from the center measured *on the plane of the disk*. The thin solid line shows the Keplerian rotation curve due to a 4.9×10^8 $M_\odot$ black hole, and the thick solid line shows the final velocity taking into account the black hole, the disk, and the stars [for $(M/L)_V = 5$]. The black hole potential dominates the velocity field in the inner $0''.5$, and we are therefore fully justified in neglecting the contribution of both stars and disk to the orbital velocity in our model. The measured velocities, corrected for the projection effects according to the best-fitting model described in the previous paragraphs, are plotted in Figure 12. As discussed for Figure 11, the black hole velocity curve due to the 4.9×10^8 $M_\odot$ black hole provides a very good fit (with $\chi^2 = 10$) to the data points, especially the ones with the smallest error bars. For comparison, the χ^2 derived from fitting a "stars only" model with $(M/L)_V = 20$ (an upper limit for a galaxy of this luminosity) is $\chi^2 = 70$; such a model can therefore be excluded on the basis of the observations.

In conclusion, the Keplerian rise in the rotational velocity revealed by the FOS spectra, implies the existence of $(4.9 \pm 1.0) \times 10^8$ $M_\odot$ inside $0''.1$ (= 14.5 pc). Integrating the V luminosity density inside this radius gives 2.3×10^5 $L_\odot$; therefore the mass-to-light ratio within the inner 14.5 pc is $(M/L)_V \sim 2130$ $M_\odot/L_\odot$. This is a very large mass-to-light ratio indeed; for comparison, $(M/L)_V$ ratios for M31 and NGC 3115, the two galaxies for which stellar dynamical studies provide the strongest evidence of the presence of a nuclear massive black hole are of the order of 100 $M_\odot/L_\odot$ and 50 $M_\odot/L_\odot$, respectively, inside $\sim 0''.3$ (Kormendy & Richstone 1992; Kormendy 1988; Kormendy et al. 1996). For M87, Harms et al. (1994) find $(M/L)_I = 170$ $M_\odot/L_\odot$ inside $0''.25$, corresponding to $(M/L)_V = 500$ $M_\odot/L_\odot$ for an elliptical galaxy with normal colors. For a typical elliptical galaxy, $(M/L)_V \sim 5$–10; therefore a normal stellar population cannot be responsible for such a large mass-to-light ratio. This combined with the presence of an active galactic nucleus, points to the conclusion that the majority of the mass is concentrated in a central black hole with $M_{\mathrm{BH}} = (4.9 \pm 1.0) \times 10^8$ $M_\odot$.

How does NGC 4261 compare to other galaxies for which the presence of a central black hole is suspected? In their recent review, Kormendy & Richstone (1995) studied black hole demographics using a sample of eight galaxies for which evidence of nuclear dark mass concentrations, possibly black holes, is found. They find a very good correlation between the black hole mass and the absolute magnitude of the bulge of the galaxy. NGC 4261 has an apparent B magnitude of 11.37 (RC3), which, at a distance of 30 Mpc, translates to an absolute blue magnitude $B = -21.0$. A black hole with mass $M_{\mathrm{BH}} = 4.9 \times 10^8$ $M_\odot$ fits the relation very well, and places NGC 4261 very close to NGC 4594 in Kormendy & Richstone's M_{BH} versus B diagram.

5. CONCLUSIONS

This paper presents a high-resolution morphological and dynamical study of the central region of the active galaxy NGC 4261, the brightest member of a small group of galaxies located at twice the distance of the Virgo cluster. *HST*/WFPC2 V, R, and I images allow a detailed study of the nuclear dust disk first detected by Jaffe et al. (1993).

The bright unresolved nucleus is surrounded by a small dust disk, about 230 pc in diameter, with nonuniform optical depth: in particular, a pseudospiral structure with lower opacity is detected extending from the nucleus to the south and north edges of the disk, probably providing the means by which angular momentum is transferred from the center outward. The disk is displaced with respect to the nucleus and the isophotal center of the galaxy, which would be the case if the disk had been acquired during a merging event and had not yet reached an equilibrium position at the center of the host galaxy, a hypothesis further supported by the observation that the disk spin axis does not coincide with the galaxy's spin axis (Davies & Birkinshaw 1986). Furthermore, the isophotal analysis shows a high degree of boxiness in the isophotes, which is often interpreted as the result of a merging event (May et al. 1985). The nucleus itself is displaced from the isophotal center of the galaxy in the direction of the radio jet, possbly due to recoil from the jet itself.

Because the R filter passband includes the Hα + [N II] spectral region, the images can be used to obtain a map of the ionized gas. The disk shows resolved Hα emission with total luminosity typical for AGNs with similar radio and X-ray fluxes (Baum & Heckman 1989; Trinchieri & di Serego Alighieri 1991). Recombination of the cooling X-ray gas does not provide enough ionizing radiation to account for the Hα luminosity; photoionization by the active nucleus and shocks, which are most likely present in the nuclear region, are likely to be the most important sources of ionization.

Spectra were obtained with the 0″.1 *HST*/FOS aperture in the spectral region between 4570 and 6870 Å, in a grid of 13 aperture positions around and at the nuclear location. [N II] λλ6548, 6584 + Hα, Hβ, [O III] λλ4459, 5007, [O I] λλ6300, 6364, [S II] λλ6717, 6731, [N I] λλ5200, 5202 and [N II] λ5756 emission lines are detected. The neutral lines of [O I] and [N I] reveal the presence of shocks. The central velocities of the [N II] lines as a function of distance from the center can be accounted for by assuming that the ionized gas is confined in a disk in Keplerian motion around a central mass $(4.9 \pm 1.0) \times 10^8\, M_\odot$. Since the mass of the underlying stellar component and the mass of the disk are several orders of magnitude smaller, they do not have a significant influence on the dynamics of the gas in the central 0″.5. We conclude that a mass $(4.9 \pm 1.0) \times 10^8\, M_\odot$ is present inside 0″.1 (=14.5 pc). Integrating the V luminosity density inside this radius gives $2.3 \times 10^5\, L_\odot$; therefore the mass-to-light ratio within the inner 14.5 pc is $(M/L)_V \sim 2130\, M_\odot/L_\odot$. For comparison. $(M/L)_V$ ratios for M31, and NGC 3115, the two galaxies for which stellar dynamical studies provide the strongest evidence of the presence of a nuclear massive black hole, are of the order of $100\, M_\odot/L_\odot$ and $50\, M_\odot$ inside ∼0″.3 (Kormendy & Richstone 1992; Kormendy 1988; Kormendy et al. 1996). For M87, Harms et al. (1994) find $(M/L)_I = 170\, M_\odot/L_\odot$, corresponding to $(M/L)_V = 500\, M_\odot/L_\odot$ inside 0″.25. The large mass-to-light ratio, and the fact that NGC 4261 *is* a relatively strong radio galaxy, lead us to conclude that the majority of the central mass is concentrated in a $(4.9 \pm 1.0) \times 10^8\, M_\odot$ black hole.

Many thanks to are due to Dr. Tony Keys, whose expertise played an essential role in planning the technical details of the *HST*/FOS observations. We are grateful to Dr. Robert O'Connell for comments on the manuscript. L. F. wishes to thank Dr. Claus Leitherer and Dr. Stephane Charlot for their invaluable help with the stellar population synthesis models. Last but not least, we wish to thank the anonymous referee for pointing out an inconsistency in the first version of this paper. L. F. received support from NASA grant GO-2227.03-87A. Support for this work was provided by NASA grant GO-05432.01-93A from the Space Telescope Science Institute, which is operated by the Association of Universities for Research in Astronomy, Inc., under NASA contract NAS 5-26555.

REFERENCES

Baum, S. A., & Heckman, T. 1989, ApJ, 336, 681

Bender, R., Surma, P., Döbereiner, S., Möllenhoff, C., & Madejsky, R. 1989, A&A, 217, 35

Birkinshaw, M., & Davies, R. L. 1985, ApJ, 291, 32

Blandford, R. D., & Rees, M. J. 1992, in Testing the AGN Paradigm, ed. S. S. Holt, S. G. Neff, & C. M. Urry (New York: AIP), 3

Bohlin, R. C., Savage, B. D., & Drake, J. F. 1978, ApJ, 224, 132

Bruzual, A. G., & Charlot S. 1993, ApJ, 405, 538

Burrows, C. J., et al. 1995, Wide Field and Planetary Camera 2 Instrument Handbook (Baltimore: STScI)

Cardelli, J. A., Clayton, G. C., & Mathis, J. S. 1989, ApJ, 345, 245

Davies, R. L., & Birkinshaw, M. 1986, ApJ, 303, L45

de Vaucouleurs, G., et al. 1991, Third Reference Catalogue of Bright Galaxies (New York: Springer) (RC3)

Ferrarese, L., van den Bosch, F., Ford, H. C., Jaffe, W., & O'Connell, R. W. 1994, AJ, 108, 1598

Farrarese, L., et al. 1996a, ApJ, 464, 568

———. 1996b, in preparation

Ford, H. C., et al. 1994, ApJ, 435, L27

Harms, R., et al. 1994, ApJ, 435, L35

Hau, G. K. T., & Tomson, R. C. 1994, MNRAS, 270, 23

Holtzman J. A., et al. 1995, PASP, 107, 156

———. 1996, in preparation

Huchra, J., Davis, M., Latham, D., & Tonry, J. 1983, ApJS, 52, 89

Jocoby, G. H., Ciardullo, R., & Ford, H. C. 1989, ApJ, 356, 332

Jaffe, W., Ford, H. C., Ferrarese, L., van den Bosch, F., & O'Connell, R. W. 1996, ApJ, 460, 214

Jaffe, W., Ford, H. C., O'Connell, R. W., Ferrarese, L., & van den Bosch, F. 1993, Nature, 364, 213

Jaffe, W., Ford, H. C., O'Connell, R. W., van den Bosch, F., & Ferrarese, L. 1994, AJ, 108, 1567

Jedrzejewski, R. I. 1987, MNRAS, 226, 747

Keyes, C. D., et al. 1995, Faint Object Spectrograph Instrument Handbook (Baltimore: STScI)

Kim, D.-W. 1989, ApJ, 346, 653

Kormendy, J. 1988, ApJ, 355, 40

Kormendy, J., & Richstone, D. 1992, ApJ, 393, 559

———. 1995, ARA&A, 33, 581

Kormendy, J., & Stauffer, J. 1987, in IAU Symp 127, Structure and Dynamics of Elliptical Galaxies, ed. P. T. de Zeeuw (Dordrecht: Reidel) 405

Kormendy, J., et al. 1996, ApJ, 459, L57

Kriss, G. A. 1994, in ASP Conf. Ser. 61, Astronomical Data Analysis Software and Systems III, ed. D. R. Crabtree, R. J. Hanisch, & J. Barnes (San Francisco: ASP), 437

Krist, J. 1995 in ASP Conf. Ser., Vol. 77, Astronomical Data Analysis Software and Systems, IV, ed. R. A. Shaw, H. E. Payne, & J. J. E. Hayes (San Francisco: ASP), 349

Lauer, T. R. 1985, ApJS, 57, 473

Lauer, T. R., et al. 1995, AJ, 110, 2622

Leitherer, C., & Heckman, T. M. 1995, ApJS, 96, 9

May, A., van Albada, T. S., & Norman, C. A. 1985, MNRAS, 214, 131

Miyoshi, M., et al. 1995, Nature, 373, 127

Möllenhoff, C., & Bender, R. 1987, A&A, 174, 63

Nolthenius, R. 1993, ApJS, 85, 1

O'Neil, E. J., Lynds, R., De Young, D. S., & Idt, W. C. 1994, BAAS, 26, 884

Osterbrock, D. E. 1989, Astrophysics of Gaseous Nebulae and Active Galactic Nuclei (Mill Valley, CA: University Science Books)

Peletier, R. F., et al. 1990, AJ, 100, 1091

Peletier, R. F., Valentijn, E. A., & Jameson, R. F. 1990, A&A, 233, 62

Richstone, D. O., & Tremaine, S. 1985, ApJ, 327, 82

Roberts, M. S., Hogg, D. E., Bregman, J. N., Forman, W. R., & Jones, C. 1991, ApJS, 75, 751

Sargent, W. L. W., et al. 1978, ApJ, 221, 731

Shklovsky, I. 1982, in IAU Symp. 97 Extragalactic Radio Sources, ed. D. S. Heeschen & C. M. Wade (Dordrecht: Reidel), 475

Trinchieri, G., & di Serego Alighieri, S. 1991, A&A, 101, 1647

van den Bosch, F., Ferrarese, L., Jaffe, W., Ford, H. C., & O'Connell, R. W. 1994, AJ, 108, 1579

Waggett, P. C., Warner, P. J., & Baldwin, J. E. 1977, MNRAS, 181, 465

Young, P. J., Sargent, W. L. W., Kristian, J., & Westphal, J. A. 1979, ApJ, 234, 76